Surface–Atmosphere Energy Exchange in an Urban Area: Insights from a Year of Eddy Covariance and Scintillometer Observations in Enschede, the Netherlands

HEET JOSHI,[a] SRINIDHI GADDE,[a] AND WIM TIMMERMANS[a]

[a] *Department of Geosciences, Faculty of Geo-Information Science and Earth Observation, University of Twente, Enschede, Netherlands*

(Manuscript received 22 December 2025, in final form 17 August 2026, accepted 2 September 2026)

ABSTRACT: Understanding urban surface–atmosphere energy exchange is key to predicting urban climate impacts. However, the heterogeneity of urban environment complicates accurate flux quantification, while multiscale, multiheight observations remain scarce. This study presents such fluxes for year 2020 using net radiometers, two-level eddy covariance (EC; neighborhood scale) and optical microwave scintillometer (SC; city scale) over Enschede, the Netherlands. Further, it evaluates the representativeness of multiscale observations, assesses flow distortion in multiheight EC measurements, and quantifies the sensitivity of SC flux estimates to input-parameter uncertainties. Results show that sensible heat Q_H follows the seasonal and diurnal cycles of net radiation, except during precipitation and high wind speeds. SC generally shows higher Q_H than EC with better temporal agreement (RMSE = 82.91 W m^{-2}; $r = 0.82$). Notable temporal differences were reported after evening. These differences likely result from a combination of factors such as uncertainties in SC input parameters, footprint mismatches between the instruments, and flow distortion effects in EC measurements. Two-height EC observations reveal flux divergence, with higher fluxes at 10 m than 5 m above the rooftop. While low-flow distortion indicated by angle of attack (AoA) and normalized turbulent kinetic energy diagnostics, the divergence highlights challenges in urban EC measurements and suggests the need for urban-specific AoA quality-control thresholds and quantification of the impact of flow distortion on fluxes. Sensitivity analyses show that SC flux estimates are affected by roughness parameters (z_0 and z_d), which exert opposing effects and may partially compensate for each other depending on local urban morphology. This dataset and analysis support satellite and NWP model validation and guide future urban flux measurements.

KEYWORDS: Atmosphere-land interaction; Urban meteorology; In situ atmospheric observations; Surface fluxes; Energy budget/balance; Morphology

1. Introduction

Urbanization is progressing rapidly worldwide, and it is estimated that 68% of the global population will reside in urban areas by 2050 (Khor et al. 2022). One of the critical consequences of this urban expansion is the significant alteration of surface properties at the local scale, such as thermal, radiative, and morphometric characteristics that modify the surface–atmosphere energy exchange. This energy exchange plays a fundamental role in driving key urban climate processes such as the urban boundary layer dynamics and the surface water and energy balance and therefore regulates air quality, heat, precipitation, and other environmental factors (Oke et al. 2017).

In urban environments, the surface energy balance (SEB) can be expressed as

$$Q^* + Q_F = Q_H + Q_E + \Delta Q_S - \Delta Q_A, \tag{1}$$

where Q^* is the net all-wave radiation, representing the net energy available at the surface, calculated as the difference between incoming and outgoing shortwave and longwave radiation; and Q_F is the anthropogenic heat flux, representing human-made heat from buildings, vehicles, industry, and metabolism. Sensible heat Q_H and latent heat Q_E are turbulent fluxes that represent turbulent transport of energy: Q_H due to vertical heat transport and Q_E due to vertical water vapor transport. Here, ΔQ_S is the net energy storage in the urban fabric, and it shows variability over diurnal and weekly time scales but marginal variation over a year (Offerle et al. 2005). Here, ΔQ_A is the net horizontal advective flux from wind-borne transport, occurring when air warmed within the densely built-up urban core is transported leeward to other areas inside or outside the city (Lowry 1977). This term is often neglected. In practice, directly measuring Q_F and ΔQ_S across entire urban canopies is troublesome due to their diffuse, nonlocalized sources and the heterogeneity of surface materials. Measuring ΔQ_A also requires a large array of sensors, making it costly and challenging in heterogeneous urban areas.

Urban SEB observations have been established in several European cities, including Basel, Marseille, Łódź, Helsinki, Essen, Oberhausen, and London (Christen and Vogt 2004; Grimmond et al. 2004; Offerle et al. 2006b,a; Fortuniak et al. 2013; Vesala et al. 2008; Weber and Kordowski 2010; Goldbach and Kuttler 2013; Kotthaus and Grimmond 2014a,b). In these observational sites, radiative fluxes are usually measured with radiometers, while turbulent fluxes are measured using the eddy covariance (EC) technique, which samples high-frequency (10–20 Hz) fluctuations of wind, temperature, and humidity linked to turbulent eddies in the atmospheric boundary layer (Aubinet et al. 2012). Despite its accuracy, the EC technique has limitations: Its footprint is generally relatively small, which

Supplemental information related to this paper is available at the Journals Online website: https://doi.org/10.1175/JAMC-D-25-0245.s1.

Corresponding author: Heet Joshi, heet.joshi@utwente.nl

DOI: 10.1175/JAMC-D-25-0245.1

© 2026 American Meteorological Society. This published article is licensed under the terms of the default AMS reuse license. For information regarding reuse of this content and general copyright information, consult the AMS Copyright Policy (www.ametsoc.org/PUBSReuseLicenses).

Brought to you by provisional account | Unauthenticated | Downloaded 11/17/26 02:09 PM UTC

gives representative fluxes of neighborhood scale and not city scale. Furthermore, fluxes must be averaged over 10–30 min to capture all relevant eddies.

Turbulent fluxes, representative of a larger footprint (on the order of a few kilometers), are crucial to quantify city-scale fluxes for validating numerical weather prediction (NWP) models and for consistent comparison with satellite data covering large areas (Li et al. 2009). Scintillometry provides such observations by transmitting optical and microwave beams whose modulation by refractive index fluctuations determines Q_H and Q_E. These dual-wavelength systems retrieve both fluxes simultaneously (Ward et al. 2015a,b). Unlike EC, the scintillometer integrates fluxes from over hundreds of meters to kilometers, efficiently captures the relevant eddies, and allows short averaging times (1 min), yielding stable, spatially representative flux estimates (De Bruin et al. 1993). This makes them highly suitable for understanding citywide flux variation, improving NWP models, and validating satellite products (e.g., Saunders et al. 2024; Rahman and Zhang 2019).

Despite the importance of urban micrometeorological observations, long-term studies combining EC and scintillometry remain scarce, and few cities worldwide host both systems, such as Swindon (Ward et al. 2014), London (Crawford et al. 2017), Łódź (Zieliński et al. 2013), and Amsterdam (Hartogensis 2026). Furthermore, studies with long-term, multiheight EC measurements are also important to understand the vertical structure of the urban boundary layer, specifically vertical flux divergence. Existing studies are often short term or focus only on one flux component, typically Q_H. To better capture the complexity of urban climates, research must expand in diverse morphologies, land uses, and climates (Arnfield 2003; Grimmond 2006), a need also emphasized by the World Meteorological Organization (Grimmond et al. 2010). The city of Enschede, in the eastern Netherlands, is among the few cities hosting both long-term EC observations at two heights (5 and 10 m above a rooftop) and scintillometer observations of both Q_H and Q_E.

This study presents such a dataset that, although available from 2018, focuses specifically on 2020. By analyzing the meteorological observations and flux estimates from both EC and scintillometer (SC), this study shows the effect of urban complexity on representativeness of flux measurements. Specifically, we report the extent of flux divergence in rooftop EC measurements and the sensitivity of SC flux estimates to key input parameters used in processing the raw SC data. Following a description of instrumentation and data processing (section 2), the results in section 3 present a full year of meteorological, radiative, and turbulent flux observations, including a comparison between EC and SC. Section 4 discusses the vertical flux divergence and flow distortion effects on EC flux measurements, and section 5 quantifies associated uncertainties and outlines methodological considerations to improve the reliability of future measurements.

2. Instrumentation and data processing

a. Measurement site

Observations are conducted in Enschede (52.22°N, 6.90°E), the largest city in the eastern Netherlands with a population of approximately 162 000 as of 2025. The city lies on a gently sloping terrain, with elevation ranging from ~60 m above mean sea level (MSL) in the east to ~30 m in the west. Enschede has a temperate oceanic climate [Köppen–Geiger classification Cfb; Kottek et al. (2006)], characterized by mild temperatures and moderate precipitation throughout the year.

Figure 1 presents the Enschede land-cover classification map based on the European Urban Atlas (Copernicus Programme 2018). The municipality is broadly divided into two zones: the inner urban core, consisting of densely built-up areas, and the outer semiurban zone, which includes a mixture of built-up and green spaces. According to land-cover data, the entire municipality comprises approximately 33.8% built-up area, 65.9% green space, and 0.3% other surface types. This work focuses on the inner urban core, defined here as the area within a radius of 2 km from the city center. Within this zone, land cover consists of approximately 84% built-up area, 12% green space, and 4% other surface types. The urban morphology is predominantly compact and midrise, with a mix of commercial and residential land use. The city center is classified according to the local climate zone (LCZ; Oke et al. 2017) as LCZ-2 (compact midrise), while the remaining urban areas encompass LCZ-2 (compact midrise), LCZ-4 (open high rise), LCZ-5 (open midrise), and LCZ-6 (open low rise). The mean building height $\overline{H}$ in the study area is around 7.12 m. Furthermore, 75% of the buildings have heights below 8.6 m, while only a few structures are exceptionally tall, such as the Alphatoren, which has a height of 101 m.

In terms of turbulent surface–atmosphere exchange, this morphology relates to aerodynamic resistance expressed with the help of so-called aerodynamic roughness length z_0 and displacement height z_d (Stull 2012). To represent the effective roughness of the city, aerodynamic z_0 and z_d were estimated using the Urban Multiscale Environmental Predictor (UMEP) roughness module (Lindberg et al. 2018), which estimates surface roughness characteristics from a digital surface model (DSM; Overheid 2020) and a digital terrain model (DTM; Overheid 2023). Using the rule of thumb method (Raupach 1994), the resulting values for z_0 and z_d are 0.8 and 5.6 m, respectively.

b. Radiation and meteorological measurements

Incoming and outgoing shortwave ($K\downarrow$ and $K\uparrow$) and longwave ($L\downarrow$ and $L\uparrow$) radiative fluxes were measured using a Kipp and Zonen CNR1 four-component radiometer (Campbell Scientific 2025a), installed on the rooftop of the ITC international hotel (52.22°N, 6.90°E), in the center of Enschede. The rooftop is approximately 46 m above ground level (AGL), with underlying terrain at ~39 m above MSL, and the four-component radiometer is mounted 2 m above the roof top (see Figs. 2a,b). These measurements enabled the calculation of net radiation Q^*, a key component of the SEB. Shortwave observations were forced to zero during the night to correct for the instrument-related nighttime offset error (Michel et al. 2008). As the radiometer is installed at 2-m height over the rooftop, it samples only the rooftop of the building and therefore radiative flux measurements are microscale in nature. Meteorological variables

Brought to you by provisional account | Unauthenticated | Downloaded 11/17/26 02:09 PM UTC

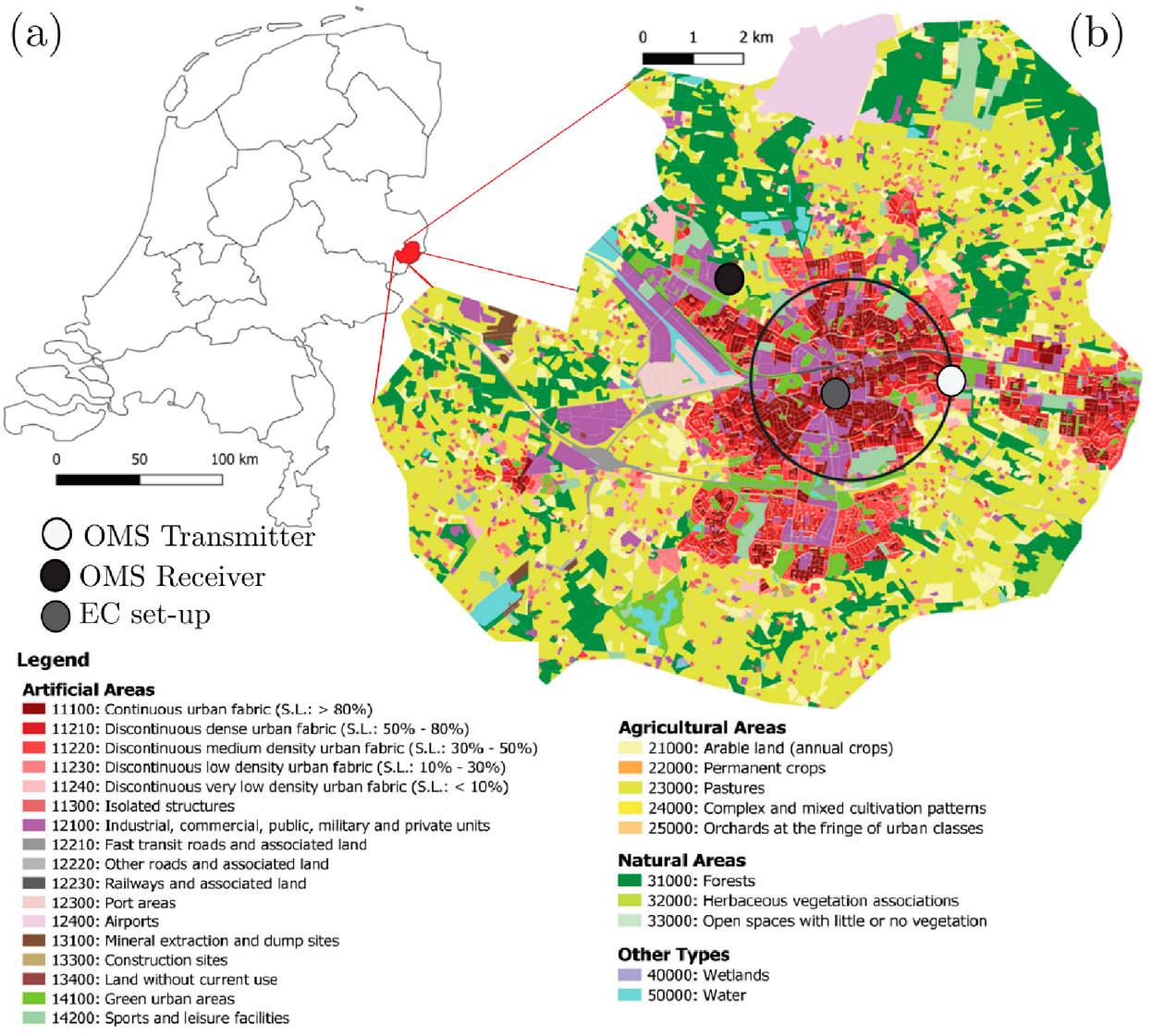


FIG. 1. (a) Location of the Enschede city in the Netherlands. (b) Land-cover classification of Enschede based on the European Urban Atlas (2018) and EC tower and OMS system location.

including air temperature [T_{air} (°C)], relative humidity [RH (%)], wind speed [u (m s^{-1})], wind direction [WD (°)], and barometric pressure [Press. (hPa)] were recorded using a Vaisala WXT520 (Vaisala 2012) integrated weather transmitter (see Figs. 2a,c), and data were recorded with a CR1000 datalogger (Campbell Scientific 2025b). Both radiative fluxes and meteorological observations were made at 1-min intervals and subsequently averaged over 30-min periods to facilitate comparison with turbulent fluxes.

c. *Precipitation and cloud cover data*

To support the interpretation of fluxes, precipitation and cloud cover data were also obtained from the nearest Royal Netherlands Meteorological Institute (KNMI) automatic weather station located at the Twente Airport (52.27°N, 6.89°E). This station is situated approximately 6 km north of the EC observation tower and provides high-quality, continuous meteorological observations. These datasets are publicly accessible via the KNMI data platform (KNMI 2020). Cloud cover data are categorized based on okta values, which range from 0 to 8. Okta values between 0 and 3 represent a clear or mostly clear sky, while higher values indicate increasing cloudiness. An okta value of 8 corresponds to a completely overcast sky. Hereafter, the data from the KNMI Twente station are marked with KNMI.

d. *Eddy covariance measurements*

Here, Q_H and Q_E at the neighborhood scale were measured using an EC system installed on the same roof top (within 20-m radius of radiation and meteorological observations) of

Brought to you by provisional account | Unauthenticated | Downloaded 11/17/26 02:09 PM UTC

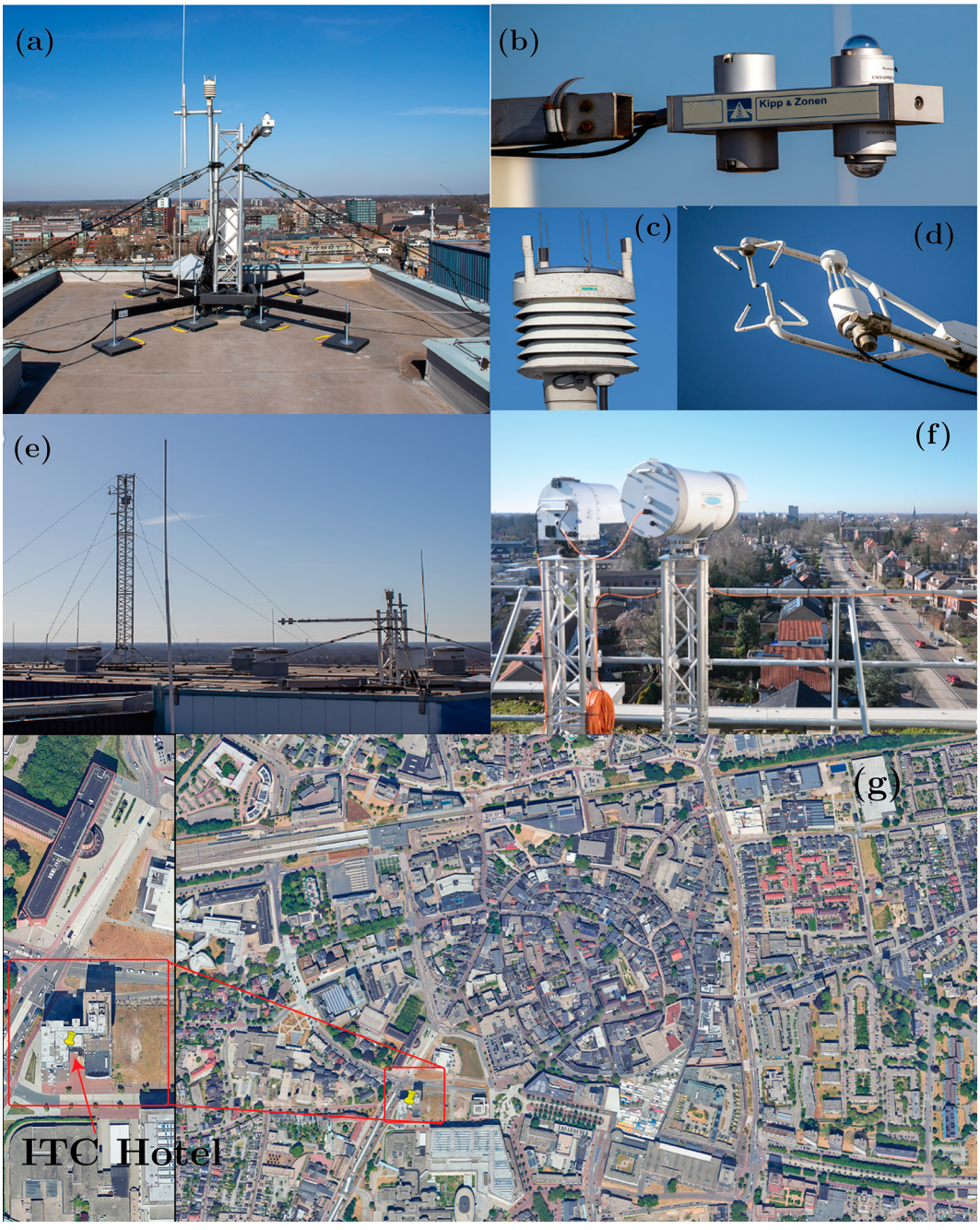


FIG. 2. Measurement setup in Enschede. (a) Four-component radiometer and weather station; (b)–(d) close ups of instruments; (e) EC tower and four-component radiometer mast on the ITC Hotel rooftop; 5-m EC setup is not in the image as it was under maintenance when the photo was taken. (f) OMS transmitter on Eschmarke flat rooftop aligned with the receiver on Horst Tower; (g) the aerial view of the city center next to the ITC Hotel (Google Earth, 2020).

the ITC international hotel (see Figs. 2e,d for the setup and Fig. 1 for the location within the city). The dual EC setup includes a 3D sonic anemometer (CSAT3, Campbell Scientific) and open-path gas analyzer (LI-7500, LI-COR) at the observation heights of 51 and 56 m AGL with north offset 225° for CSAT3. These instruments record high-frequency (10 Hz) time series of three components of wind speed (u, v, w), sonic temperature (θ_s), and water vapor (q). The values of Q_H and Q_E are estimated from correlation between the fluctuations of w and θ (air temperature, obtained by applying the humidity correction to the θ_s) and w and q, respectively. Fluctuations are calculated by subtracting the 30-min block averages, i.e., $w' = w - \overline{w}$, $\theta' = \theta - \overline{\theta}$, and $q' = q - \overline{q}$, where the prime represents fluctuations and the overbar represents the

Brought to you by provisional account | Unauthenticated | Downloaded 11/17/26 02:09 PM UTC

block average. Further, Q_H and Q_E are calculated using the covariance method as follows:

$$Q_H = \rho c_p \overline{w'\theta'} \quad \text{and} \quad Q_E = \rho L_v \overline{w'q'}, \tag{2}$$

where ρ is the air density (kg m^{-3}), c_p is the specific heat capacity of air at constant pressure (J kg^{-1} K^{-1}), and L_v is the latent heat of vaporization (J kg^{-1}).

The high-frequency raw data were recorded using a CR3000 datalogger and processed with EddyPro software. Coordinate rotation was applied using the double-rotation method following Kaimal and Finnigan (1994). Spectral corrections were performed to account for signal attenuation across frequency ranges: Low-frequency losses were corrected using the analytic correction for high-pass filtering effects (Moncrieff et al. 2004), while high-frequency losses were corrected using the fully analytic method described by Moncrieff et al. (2004). Turbulent fluctuations were extracted from the time series using the block-averaging method, and time lag compensation between scalar and vertical wind measurements was carried out using the covariance maximization method in EddyPro. Quality control followed the methodology described by Winck et al. (2023), applying the flagging scheme of Foken et al. (2004), with only high-quality (flag 0) and acceptable (flag 1) data retained, filtering values outside physically plausible ranges and removing outliers exceeding 3 times the standard deviations from a 30-min moving average with a moving 3-day window. By applying this quality control, we discard 11.8% and 19% of the actual data for Q_H and Q_E, respectively.

We note here that previous studies have shown that EC measurements above the rooftop of a tall building can be subjected to flow distortion effect (Feigenwinter et al. 2012; Barlow et al. 2011), and nonparallel alignment of the mean streamline with the ground surface can introduce errors in flux estimation (Finnigan et al. 2003). Specifically over rooftop observations, such misalignment commonly arises from flow separation and deflection around and above the building itself and nearby buildings. This effect can be identified based on the comparison between two-level EC fluxes (vertical flux divergence), the angle of attack (AoA), and normalized turbulent kinetic energy ($\text{TKE}_{\text{Nor.}}$) (Grimmond et al. 2004; Feigenwinter et al. 2012; Järvi et al. 2018; Horne et al. 2026). Our rooftop flux observations show such a flux divergence with nonzero AoA. There is no consensus on acceptable AoA values for the urban area, and different studies apply varying quality-control criteria (e.g., Järvi et al. 2018; Horne et al. 2026). However, Feigenwinter et al. (2012) report mean AoA values varying between −50° and 20° in certain flow sectors for measurements over the rooftop of isolated high-rise buildings showing high flow distortion whereas an EC system on 20-m lattice tower on top of a 20-m tall building, they obtain AoA varying between −20° and 5° showing lower flow distortion. The AoA observed at Enschede rooftop measurements ranges from −5° to 15°, consistent with the range reported by Feigenwinter et al. (2012) as exhibiting low flow distortion. Therefore, in this study, we apply filtering and retain only data with $|\text{AoA}| < 15°$. A detailed analysis of the flux divergence is presented in section 5.

e. Optical microwave scintillometer

To obtain Q_H and Q_E at the city scale, a dual-wavelength scintillometer system RPG-MWSC-160, comprising an optical beam (wavelength 0.88 μm) and a microwave beam (wavelength 1860 μm), was deployed across Enschede (see Fig. 2f for instrumental setup and Fig. 1 for transmitter and receiver locations). The transmitter was installed on the rooftop of the Eschmarke tower (~31 m AGL) in the eastern side of the city, and the receiver was installed on the Horst Tower (~52 m AGL) at the University of Twente campus in the western side of the city. The 4.9-km path primarily samples the Enschede central urban area due to the path-weighting function of the optical microwave scintillometer (OMS) system, which has higher weight near the path center than at the transmitter and receiver ends.

The OMS setup enables the retrieval of path-averaged Q_H and Q_E by measuring refractive index fluctuations caused by temperature and humidity variations. Estimation of the fluxes includes three processing steps. First, the structure parameter of the refractive index for the optical $[C^2_{n,\text{opt}}(\text{m}^{-2/3})]$, microwave $[C^2_{n,\text{mw}}(\text{m}^{-2/3})]$, and an additional combined structure parameter $[C^2_{n,\text{opt,mw}}(\text{m}^{-2/3})]$ are derived from log-intensity fluctuations measured at the receiver (Radiometer Physics 2018). The second step involves the calculation of the structure parameter of temperature $[C^2_T(\text{K}^2\,\text{m}^{-2/3})]$, humidity $[C^2_q(\text{kg}^2\,\text{kg}^{-2}\,\text{m}^{-2/3})]$, and the temperature–humidity covariance C_{Tq} (K kg kg^{-1} m$^{-2/3}$) using the bichromatic method described by Lüdi et al. (2005). In the final step, Monin–Obukhov similarity theory (MOST; Monin and Obukhov 1954) is applied to estimate the turbulent fluxes, where the similarity functions (i.e., $f_{C^2_T}$ and $f_{C^2_q}$) relate to the structure parameters as follows:

$$f_{C^2_T} = \frac{z^{2/3} C^2_T}{T^2_*} \quad \text{and} \quad f_{C^2_q} = \frac{z^{2/3} C^2_q}{q^2_*}, \tag{3}$$

where z is the measurement height, given by $z = z_{\text{eff}} - z_d$, and T_* and q_* are the scaling variables for temperature and humidity, respectively. Here, the effective height z_{eff} is calculated as follows (Hartogensis et al. 2003):

$$z_{\text{eff}} = \frac{-1 + \sqrt{1 - \frac{4c}{L_o}\left(\int_0^1 \left\{ Z(x)\left[1 - \frac{cZ(x)}{L_o}\right]\right\}^{-2/3} G(x)dx\right)^{-3/2}}}{-\frac{2c}{L_o}}, \tag{4}$$

where $Z(x)$ represents the beam height along the path, L_o is Monin–Obukhov length, and $G(x)$ is the scintillometer path-weighting function, which differs between the LAS and MWS systems. The parameter c is an empirical stability coefficient, taking the value $c = 6.1$ under unstable atmospheric conditions and $c = 2.2$ under stable conditions (Ward 2017). For the OMS system, the effective height is taken as the average of the individual LAS and MWS effective heights:

$$z_{\text{eff}} = 0.5(z^{\text{LAS}}_{\text{eff}} + z^{\text{MWS}}_{\text{eff}}). \tag{5}$$

Brought to you by provisional account | Unauthenticated | Downloaded 11/17/26 02:09 PM UTC

For solving Eq. (7), several forms of similarity functions relating structure parameters of temperature and humidity with the structure parameter of refractive indices are available in the literature (e.g., Andreas 1988; Li et al. 2012). In this study, the coefficients proposed by Andreas (1988) are adopted, as they are widely used in urban scintillometer literature (Lagouarde et al. 2006; Ward et al. 2014, 2015b; Crawford et al. 2017) and facilitate the comparison of the results with other studies. This consistency is important since the use of different similarity functions can result in flux estimates that differ by as much as ±30% during unstable conditions (Ward 2017). Consistent with previous studies (Ward 2017), identical similarity functions are assumed for temperature and humidity, with coefficients $c_1 = 4.9$, $c_2 = 6.1$, and $c_3 = 2.2$. Accordingly, we have

$$f_{C_T^2}, f_{C_q^2} = f\left(\frac{z}{L_o}\right) = \begin{cases} c_1\left[1 - c_2\left(\frac{z}{L_o}\right)\right]^{-2/3}, & \text{for unstable conditions,} \\ c_1\left[1 + c_3\left(\frac{z}{L_o}\right)^{2/3}\right], & \text{for stable conditions.} \end{cases} \tag{6}$$

The scaling variables obtained from Eq. (3) are related to Q_H and Q_E as follows:

$$Q_H = -\overline{\rho} c_p u_* T_* \quad \text{and} \quad Q_E = \frac{-\overline{\rho} L_v u_* q_*}{(1 - \overline{q})}, \tag{7}$$

where $\overline{q}$ represents the mean specific humidity (kg kg^{-1}) and u_* represents the friction velocity. From Eq. (7), it is clear that u_* is required as an input to estimate Q_H and Q_E. Also, u_* is typically estimated from the meteorological inputs using

$$u_* = \frac{\kappa u}{\ln\left(\frac{z_u - z_d}{z_0}\right) - \Psi_m\left(\frac{z_u - z_d}{L_o}\right) + \Psi_m\left(\frac{z_0}{L_o}\right)}. \tag{8}$$

Here, u is the wind speed, z_u is the height at which u is measured, Ψ_m represents the stability correction function, and κ is the von Kármán constant. The scintillometer's receiver and transmitter were placed at the edge of the city to cover the entire urban area. Since the land cover in the location of the transmitter and receiver is semiurban and not representative of the meteorological conditions of the city center, meteorological data for scintillometer processing were obtained from the rooftop observations at the ITC hotel which is more appropriate as an urban meteorological input. The final flux estimates from Eq. (7) are sensitive to the location of the meteorological input, and this is discussed in section 5b. The stability correction functions $\Psi_m(z/L_o)$ and $\Psi_m(z_0/L_o)$ are defined as follows (Hartogensis 2006):

$$\Psi_m\left(\frac{z_u - z_d}{L_o}\right) = \begin{cases} 2\ln\left(\frac{1 + x_m}{2}\right) + \ln\left(\frac{1 + x_m^2}{2}\right) + \tan^{-1}(x_m) + \frac{\pi}{2}, & \left(\frac{z_u - z_d}{L_o} < 0\right), \\ 1 - \left(1 + 6.25\frac{z_u - z_d}{L_o}\right)^{4/5}, & \left(\frac{z_u - z_d}{L_o} \geq 0\right), \end{cases} \tag{9}$$

with

$$x_m = \left(1 - 16\frac{z_u - z_d}{L_o}\right)^{1/4}. \tag{10}$$

Substituting Eq. (6) into Eq. (3), the scaling variables can be obtained within an iterative framework to estimate Q_H and Q_E from Eq. (7). The procedure typically begins with an initial guess of the L_o which is subsequently updated using

$$L_o = -\frac{u_*^2 \overline{T}}{g\kappa T_*\left(1 + 0.07\frac{Q_E}{Q_H}\right)}, \tag{11}$$

where κ is von Kármán constant and g is the gravitational acceleration. The z_{eff} is likewise determined iteratively with L_o.

The OMS system utilizes the cospectrum to derive correlated structure parameter C_{Tq}, enabling direct estimation of the correlation coefficient as follows:

$$R_{Tq} = \frac{C_{Tq}}{(C_T^2 C_q^2)^{1/2}}. \tag{12}$$

This coefficient ranges from −1 to +1 and quantifies the linear correlation between temperature and humidity fluctuations. In the classical two-wavelength approach, R_{Tq} is prescribed as +1 under unstable atmospheric conditions and −1 under stable conditions (Hill 1997). Physically, R_{Tq} has the same sign as the product of Q_H and Q_E. Negative Q_H is typically associated with stably stratified conditions, whereas negative Q_E arises from dew formation. However, even when Q_E flux becomes negative, its magnitude is generally small. For

Brought to you by provisional account | Unauthenticated | Downloaded 11/17/26 02:09 PM UTC

this reason, the RPG–MWSC scintillometer data processing software assumes a consistently positive Q_E flux. Under this assumption, R_{Tq} uniquely determines the sign of Q_H (Radiometer Physics 2018). The fluxes are derived at 1-min intervals. Similar to the EC data, flux values exceeding 3 times the standard deviation from the moving average were discarded, and the data were averaged to a 30-min interval to facilitate comparison.

f. Footprint calculation

Turbulent flux measurements represent a certain source area influenced by sensor height, u, WD, atmospheric stability, land cover, and aerodynamic roughness parameters. To spatially contextualize the flux observations, knowing this source area or footprint area is essential. For the EC system, a two-dimensional parameterization based on the flux footprint prediction (FFP) model by Kljun et al. (2015) was applied. This model estimates the upwind source area contributing to measured fluxes, based on micrometeorological inputs and surface characteristics.

For the scintillometer, along the 4.9-km path, pointwise footprints were calculated at every 40-m interval between the transmitter and receiver. At each point, the FFP model was applied, and the resulting normalized footprints were then weighted using the OMS's path-weighting function to obtain a spatially distributed flux footprint for the scintillometer, following the approach of Meijninger et al. (2002).

For the FFP model, estimates of surface aerodynamic roughness parameters (z_0 and z_d) are required in addition to observed micrometeorological variables. These parameters were derived using UMEP by opting for the rule-of-thumb method. For each point of interest, a 500-m radius buffer was delineated and subdivided into 10° angular sectors. The sector corresponding to the prevailing WD was then used to compute the spatially variable roughness parameter. This procedure allows to account for both the spatial and directional variability of the surrounding urban morphology.

3. Results

a. Meteorology

In the year 2020, Enschede exhibited the typical seasonal pattern of temperate climate (Fig. 3). Winter (DJF) was typically cold and wet. Spring (MAM) was mild (Fig. 3a) and the driest season (Fig. 3e). Summer (JJA) was the warmest (maximum 34.5°C in early August) with the second-highest precipitation. Specifically, precipitation in June was more intense early in the month, while in July, it was more evenly distributed through the month. Autumn (SON) was mild with moderate precipitation. Spring had the most clear-sky days, whereas winter was mostly overcast (Table 1). The annual mean T_{air} for the year 2020 (Table 1) was 12.2°C, slightly above the national mean (11.7°C; Huiskamp 2021) and past 30-yr (1990–2019) mean (10.1°C). Mean RH (Table 1) was 67% (higher in winter, lower in summer). Mean u (Table 1) was 2.9 m s^{-1}, lower than the 30-yr mean (3.5 m s^{-1}; Table 1). Annual precipitation totaled 687, ~98 mm below the national and 96.4 mm below past 30-yr average; winter was wettest, and spring was driest. The WD was mainly southerly in winter and autumn (Fig. 4). Spring was more variable [northwest–northeast (NE) dominant; ~25% south (S)-southwest (SW)]. In summer, ~50% of the winds were S-SW. Diurnal cycles of T_{air} and RH (not shown) were weak in winter but pronounced from spring to autumn, with afternoon temperature maxima and RH minima. The u peaked around midday and was lowest at night, with the strongest diurnal contrast outside winter.

b. Radiative fluxes

1) Shortwave radiation

The $K\downarrow$ exhibits the typical annual sine pattern, with a minimum in January and a maximum in July, despite cloud variability (Fig. 5a). Variations are primarily driven by solar elevation, day length, and cloud cover. The $K\uparrow$ shows a similar pattern as $K\downarrow$, with slight modulation by changes in albedo due to solar angle and surface moisture (Table 2). The annual (24 h) mean $K\downarrow$ and $K\uparrow$ values were 127 and 24 W m^{-2}, respectively. The annual mean α was 0.21, remaining relatively stable seasonally with a slight decrease in winter, consistent with the effect of higher precipitation prolonging surface moisture as wet surfaces generally exhibit lower albedo than dry surfaces (Tirel et al. 2025).

Airborne remote sensing observations within a 500-m radius of the ITC building show considerable spatial variability in rooftop albedo, ranging from 0.03 to 0.495. This variability reflects differences in roofing materials, roof age, and surface conditions across the surrounding urban area. To characterize the neighborhood, the mean rooftop albedo was calculated from 351 rooftop samples, resulting in an average value of 0.10. In comparison, the annual mean rooftop albedo measured at the ITC rooftop using the four-component radiometer is 0.21, showing that the ITC rooftop is more reflective than the average rooftop in the surrounding neighborhood. However, the comparison between airborne and ground-based estimates should be interpreted with appropriate consideration of their different measurement characteristics. Even for the ITC rooftop itself, the airborne retrieval yields an albedo of 0.15, compared with an annual mean of 0.21 and a monthly median of 0.19 for the same time of the day from the four-component radiometer. This difference might be because the four-component radiometer measures an annual mean hemispherical broadband albedo, whereas the airborne product is an instantaneous retrieval acquired around afternoon time on a single day and is derived from directional reflected radiance. Consequently, the airborne estimate is influenced by solar-view geometry, illumination conditions, subpixel surface heterogeneity, and the three-dimensional structure of the urban environment.

The relatively high albedo of the ITC rooftop is primarily attributed to its relatively high reflective roofing material, which can be seen clearly from Fig. 2a. This roofing material differs from the darker roof surfaces that are more commonly found in the Netherlands, where reported rooftop albedo values typically range from 0.06 to 0.16 in Rotterdam and average approximately 0.158 in Delft (Klok et al. 2012;

Brought to you by provisional account | Unauthenticated | Downloaded 11/17/26 02:09 PM UTC

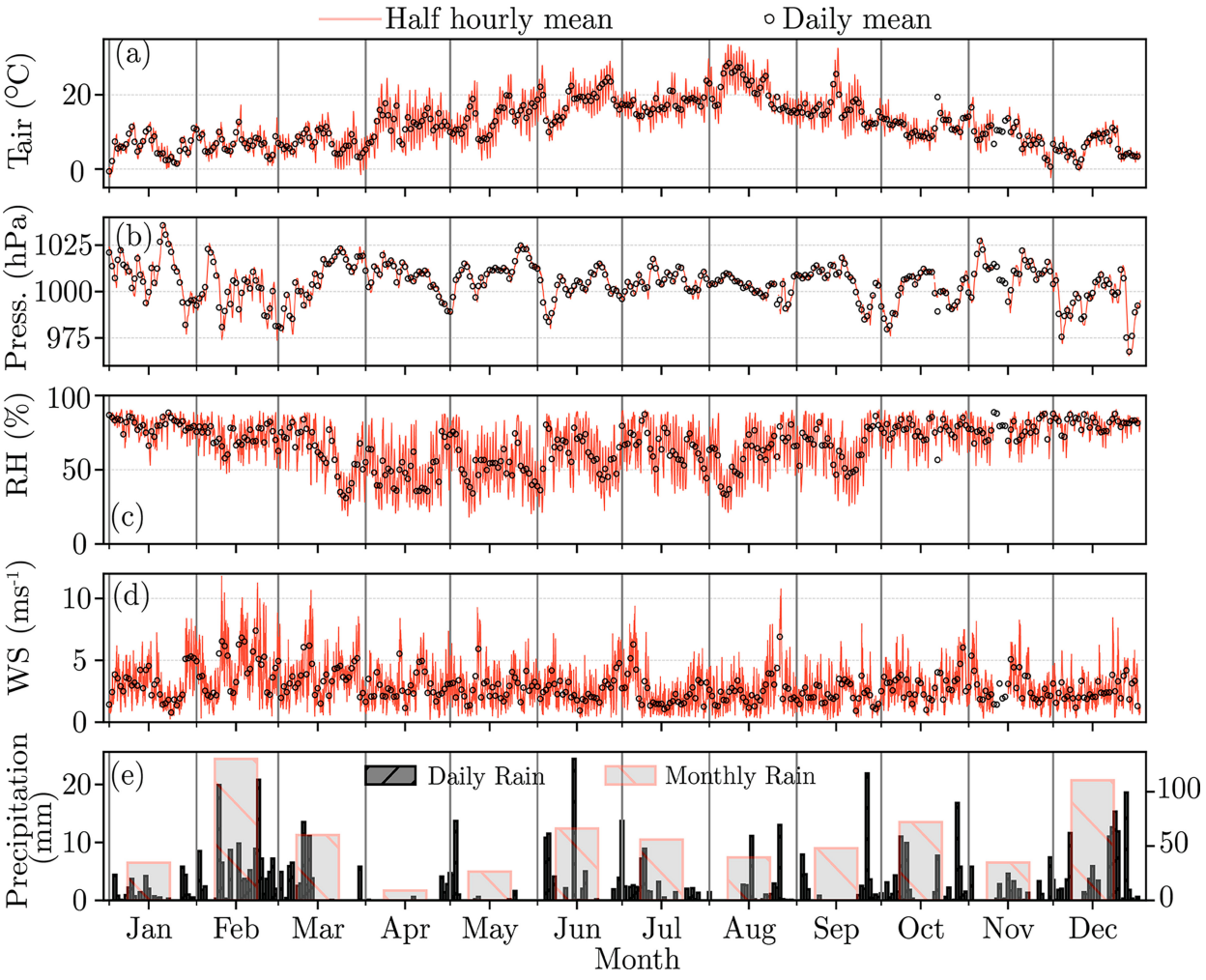


FIG. 3. Meteorological observations: (a) T_{air}, (b) pressure, (c) RH, (d) u, and (e) precipitation (KNMI) for daily (left axis) and monthly (right axis).

Zhou et al. 2025). Consequently, because the ITC rooftop is more reflective than the surrounding neighborhood, the measured $K\uparrow$ and, by extension, Q^* may therefore not be fully representative of neighborhood-scale conditions. The mean $K\downarrow$ shows a strong seasonal increase, rising from approximately 27 W m^{-2} in winter to values exceeding 200 W m^{-2} in summer, and provides the primary radiative energy input to the urban surface.

TABLE 1. Seasonal statistics of meteorological variables. All variables are averaged, except precipitation which represents the total precipitation.

Meteorological parameters	Past 30 years (KNMI)	Annual	Winter	Spring	Summer	Autumn
T_{air} (°C)	10.1	12.2	6.2	10.9	19.1	12.2
RH (%)	81	67.15	78.4	55.1	62.2	73.1
u (m s^{-1})	3.5	2.9	3.2	3.1	2.5	2.7
Total precipitation (KNMI; mm)	783.4	687.1	275.3	95.5	161.5	154.8
Cloud condition (KNMI) % of daytime						
Clear (okta: 0–3)	—	—	6	37	21	22
Partially and fully overcast (okta: 4–8)	—	—	94	63	79	78
Cloud condition (KNMI) % of nighttime						
Clear sky (okta: 0–3)	—	—	9	38	29	25
Partially and fully overcast (okta: 4–8)	—	—	81	62	71	75

Brought to you by provisional account | Unauthenticated | Downloaded 11/17/26 02:09 PM UTC

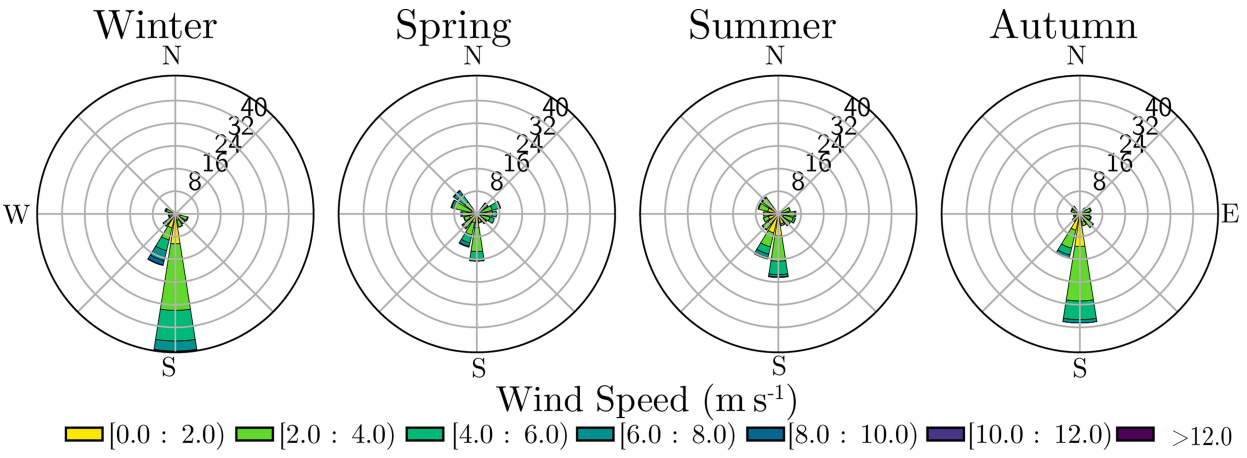


FIG. 4. Seasonal wind roses showing the frequency and direction of prevailing winds.

2) LONGWAVE RADIATION

The $L\downarrow$ is primarily controlled by T_{air} and the emissivity of atmosphere ϵ_a. Cloud cover, especially low- and midlevel clouds, strongly enhances $L\downarrow$ because clouds are efficient infrared emitters (Flerchinger et al. 2009). Accordingly, the temporal evolution of $L\downarrow$ closely follows variations in T_{air} and atmospheric moisture content. The annual mean $L\downarrow$ was 299 W m^{-2}. Seasonally, it is lowest in spring due to clear skies and moderate T_{air} and highest in summer when T_{air} is elevated. Despite low T_{air}, winter exhibits moderately high $L\downarrow$ as a result of frequent cloud cover and higher humidity.

The $L\uparrow$ is mainly governed by surface skin temperature T_s and rooftop material properties, with minor contributions from conductive and convective processes (Kotthaus and Grimmond 2014a). The annual mean $L\uparrow$ was 357 W m^{-2}. The $L\uparrow$ is lowest in winter and highest in summer, reflecting the influence of net solar input on T_s. The maximum value occurs in August (415 W m^{-2}), and the minimum value occurs in December (313 W m^{-2}).

3) NET RADIATION Q^*

Figure 5f presents the variability of Q^* over the year. The annual mean Q^* was 44 W m^{-2}, indicating a net radiative energy gain at the site. Seasonal means (Table 2) indicate negative values in winter, high positive values in summer, and intermediate values in spring and autumn. Monthly median diurnal patterns (Fig. 7a) of Q^* show low variation during the colder months (October–February) due to low solar input and more pronounced variation during the warmer months (March–September). Nighttime values were negative year-round, with more negative values during less-cloudy months and less negative or zero values in more-cloudy months. Although the microscale footprint of the four-component radiometer introduces uncertainty in flux magnitudes, the seasonal and diurnal structure of Q^* with negative fluxes in winter, strongly positive in summer, with pronounced daytime peaks in warmer months establishes the first-order temporal variability that governs turbulent energy partitioning which is discussed in the following section.

c. *Turbulent fluxes*

In this section, we discuss the general trends of the turbulent fluxes from the scintillometer (Q_{H_SC} and Q_{E_SC}) and eddy covariance (Q_{H_EC} and Q_{E_EC}). Here, the analysis focuses on EC fluxes from the instrument at 10 m above the rooftop for two primary reasons. First, measurements at 10 m represent a larger source footprint than those at 5 m, which is better for comparison with scintillometer observations. Second, the analysis of flow distortion and flux divergence (discussed in section 4) indicates that the measurements from 5 m have greater sensitivity than those from 10 m to nearby roughness elements.

1) SEASONAL VARIABILITY

Both Q_{H_SC} (Fig. 6b) and Q_{H_EC} (Fig. 6d) broadly follow the temporal evolution of Q^* (Fig. 6a). Average turbulent fluxes (Table 3) are lowest during winter, primarily due to reduced Q^* and consequently limited available energy. During this period, the partitioning between Q_H and Q_E reflects the influence of the season with highest precipitation and strongest winds (Table 1). Precipitation increases surface water availability, causing a larger fraction of the available energy to be partitioned into Q_E to support evaporation. Stronger winds enhance turbulent exchange, which further promotes evaporation. Consequently, Q_E dominates, while Q_H remains small or negative.

During spring, increasing Q^* and persistently high wind speeds support a sharp rise in turbulent fluxes. As spring is the driest season (Fig. 3e), the available energy is preferentially partitioned into Q_H, making it the dominant component. In summer, turbulent fluxes reach their maximum (Table 3). The increased precipitation of this season and potentially more actively growing vegetation promote stronger Q_E contributions (Fig. 6f), resulting in a more balanced partitioning between Q_H and Q_E, as evident from β_{SC} and β_{EC} (Table 3).

Brought to you by provisional account | Unauthenticated | Downloaded 11/17/26 02:09 PM UTC

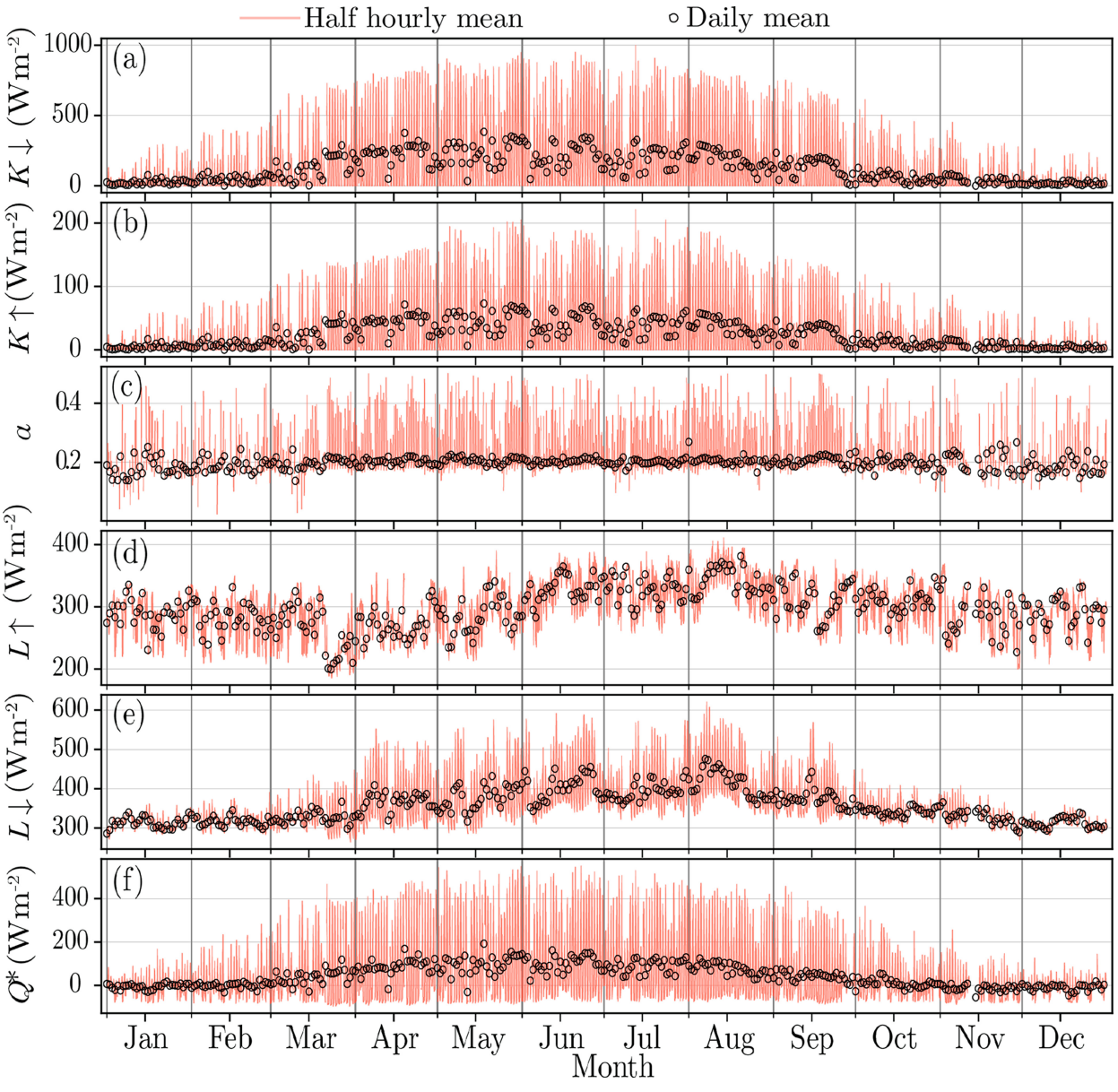


FIG. 5. Radiative flux (W m^{-2}) and albedo measurements: (a) $K\downarrow$, (b) $K\uparrow$, (c) α, (d) $L\uparrow$, (e) $L\downarrow$, and (f) Q^*.

During autumn, fluxes are moderate (Table 3), with values between those of winter and spring.

The influence of synoptic meteorological conditions is clearly evident at finer time scales. During several periods, including February, early July, and late August, Q_H occasionally becomes negative or only weakly tracks Q^* (Figs. 6a–c). These periods provide examples of how strong winds and precipitation events (Figs. 3d,e) influence energy partitioning by enhancing Q_E (Figs. 6d,e) and consequently reducing Q_H. In most cases, higher wind speeds and heavy precipitation events tend to occur simultaneously (Figs. 3d,e), consistent with synoptic-scale meteorological dynamics. Examples of such concurrent events occur in February, early March, early June and July, late August, and late December.

2) DIURNAL PATTERNS

Figure 7 presents the monthly median diurnal patterns of turbulent fluxes compared to Q^*. During warmer months (March–September), the turbulent fluxes exhibit a clearer diurnal cycle that broadly corresponds with the daytime evolution of Q^* (Figs. 7a–c). During colder months (October–February), the correspondence between the turbulent fluxes and Q^* is less apparent, which may be attributed, at least in part, to the relatively weak diurnal variation in Q^* itself.

The diurnal patterns of Q_H observed by both EC and SC show similar trends: The Q_H increases in the morning as Q^* rises, peaks around noon, and then decreases as Q^* diminishes. During warmer months, Q_{H_SC} exhibits a wider diurnal

Brought to you by provisional account | Unauthenticated | Downloaded 11/17/26 02:09 PM UTC

TABLE 2. Seasonal mean radiative flux observations.

Radiative fluxes (W m^{-2})	Annual average (24 h)	Winter	Spring	Summer	Autumn
$K\downarrow$	127	27	196	202	78
$K\uparrow$	24	5	37	39	15
$L\downarrow$	299	288	272	332	302
$L\uparrow$	357	314	356	404	349
Q^*	44	−4	74	90	15

range, with higher magnitude daytime flux and more negative flux from evening to midnight than Q_{H_EC} (Fig. 7b). Specifically, Q_{H_SC} exhibits consistent negative fluxes during nighttime, while fluxes of Q_{H_EC} are nearly zero.

As mentioned previously, EC fluxes are possibly affected by the flow distortion due to the building which could cause the differences in the magnitude of the fluxes which is discussed further in section 4. Nonetheless, there can be other possible causes for the difference between Q_{H_SC} and Q_{H_EC}, for example, flux footprint. At Enschede, SC footprint contains a lower fraction of built-up surfaces than the EC footprint (Table 4a). Due to lower thermal inertia, non-built-up surfaces heat up more rapidly during the day, producing higher Q_H, and cool more quickly, leading to stronger negative values. In contrast, the EC footprint includes a higher built-up fraction; urban materials typically have higher heat storage capacity, which can delay the daytime Q_H increase and result in lower daytime peaks. The stored heat is gradually released at night, reducing the magnitude of negative Q_H. Additionally, the more negative values of Q_{H_SC} from late evening to midnight may partly reflect enhanced energy redistribution toward Q_E. This is consistent with the observation that Q_{E_SC} shows persistent positive values during this time, likely due to the greater presence of vegetated surfaces within the SC footprint sustaining evapotranspiration. In contrast, the EC footprint, characterized by a high built-up fraction, shows lower Q_E values due to weaker evapotranspiration. Furthermore, Q_{H_SC} after midnight time tends to remain nearly constant or exhibit a slight continuous increase (Fig. 7b). This apparent increase is related to the determination of the sign of Q_H from the bichromatic-correlation approach. In the retrieval, the sign of Q_H is inferred from the sign of r_{Tq} (or equivalently C_{Tq}). However, a positive r_{Tq} during nighttime does not uniquely imply a positive sensible heat flux. The positive nocturnal r_{Tq} can occur under stable conditions with $Q_H < 0$ and $Q_E < 0$, for example, during dew fall (Ward et al. 2015b). Because r_{Tq} describes the relative sign of the two fluxes, the bichromatic-correlation method cannot distinguish this case from $Q_H > 0$ and $Q_E > 0$ solely from the

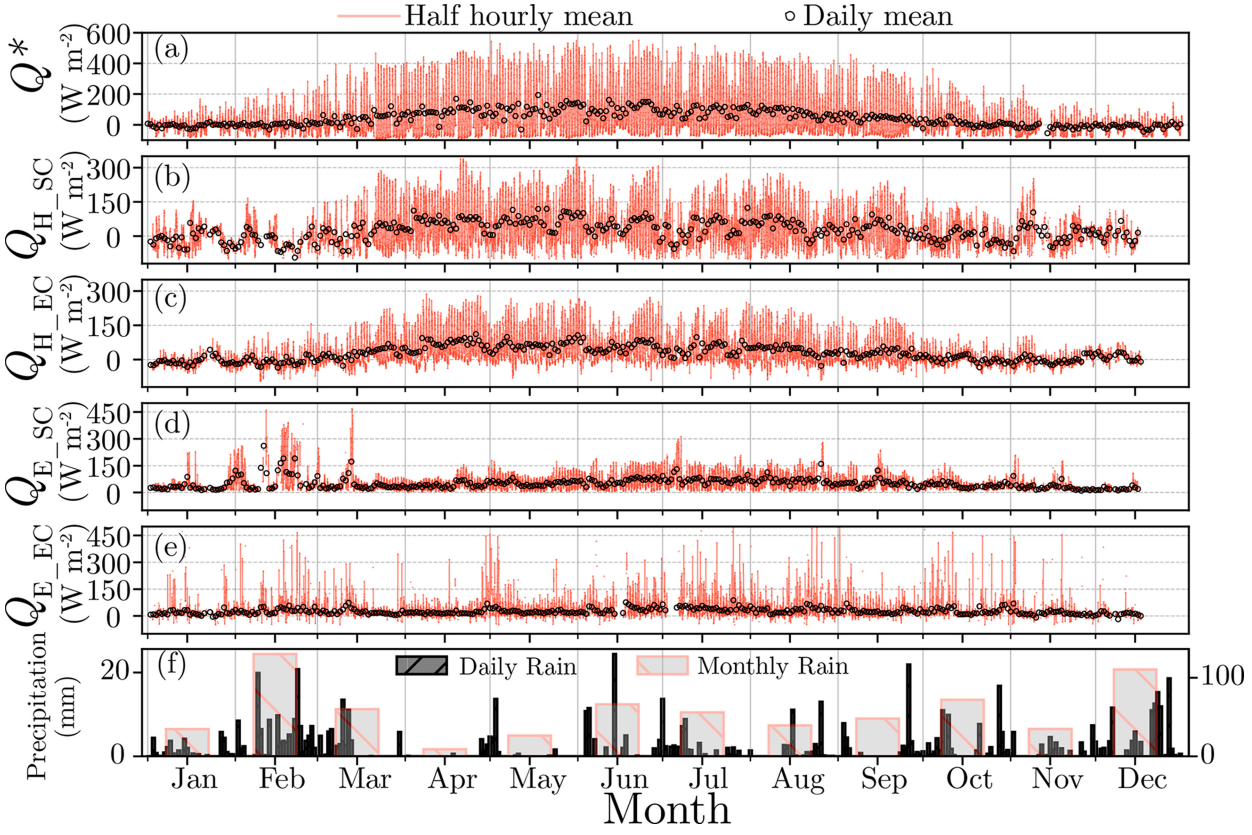


FIG. 6. Net radiation (W m^{-2}), turbulent fluxes (W m^{-2}), Bowen ratio, and precipitation: (a) Q^*, (b) Q_{H_SC}, (c) Q_{H_EC}, (d) Q_{E_SC} (10 m), (e) Q_{E_EC} (10 m), and (f) precipitation (mm).

Brought to you by provisional account | Unauthenticated | Downloaded 11/17/26 02:09 PM UTC

TABLE 3. Seasonal mean: net radiation and turbulent flux observations.

Energy fluxes (W m^{-2})	Annual average (24 h)	Winter	Spring	Summer	Autumn
(Q_{H_SC} + Q_{E_SC})	108 (44 + 64)	52 (−1 + 52)	142 (82 + 60)	163 (72 + 91)	75 (23 + 52)
(Q_{H_EC} + Q_{E_EC})	52 (26 + 26)	17 (−5 + 22)	74 (52 + 22)	85 (48 + 37)	32 (9 + 23)
Q^*	44	−4	74	90	15
		Bowen ratio (β)			
β_{SC}	0.311	0.098	0.654	0.400	0.092
β_{EC}	0.664	−0.419	1.848	1.013	0.213

sign of r_{Tq}. Therefore, Ward et al. (2015b) treated nocturnal $r_{Tq} > 0$ as indicative of dew fall. In addition, the sign of C_{Tq}, and consequently r_{Tq}, becomes particularly uncertain under weak nocturnal turbulence because the absolute values of C_{Tq} and C_q^2 are small. The uncertainty in r_{Tq} is especially pronounced during nighttime and transition conditions, when the relevant structure parameters become small. Thus, small fluctuations in C_{Tq} around zero can result in a change in the inferred sign of r_{Tq}, which can in turn reverse the inferred sign of the heat flux (Beyrich et al. 2005). This interpretation is also consistent with the abrupt change in the retrieved nighttime signal from negative to positive values in April and May, while the magnitude remains comparable. Such a sign reversal is more consistent with an ambiguity or uncertainty in the inferred flux sign than with a physical discontinuity in the nighttime heat flux.

3) FLUX FOOTPRINT CHARACTERISTICS

To better interpret the differences between SC and EC fluxes, it is essential to consider their respective flux footprints. Representative four clear-sky days were selected, each corresponding to one of the dominant wind directions observed at the Enschede site, as identified from the 10-m EC wind rose. This wind rose differs from that shown in Fig. 4, which is based on the 2-m WXT520 measurements; the reasons for these differences are briefly discussed in section 5b. For each day and each 30-min interval, the footprint was calculated for both EC and SC.

We selected 21 April, 5 May, 11 August, and 20 August, with mean daily WDs representing NE, north (N), east (E), and S-SW, respectively. Figure 8 presents example footprints at 1200 local time. In Fig. 8a, yellow contours correspond to northerly flow and red contours correspond to easterly flow, while in Fig. 8b, red contours indicate northeasterly flow and yellow contours represent southwesterly flow. Each contour represents footprint contributions ranging from 70% to 90%. Table 4a presents the footprint-weighted mean land-cover characteristics of the EC and SC for the entire day, considering only unstable and neutral conditions. Table 4b includes the mean building height $\overline{H}$, standard deviation of building height σ_H, and maximum building height H_{Max} within the footprint. The building statistics ($\overline{H}$, σ_H, and H_{Max}) were calculated using the building pixels located within the footprint of EC and SC.

From Table 4a, the surface characteristics within each footprint show minimal variation across dominant WDs, indicating that the heterogeneity of surface characteristics is relatively stable for each instrument site. However, comparing EC and SC footprints reveals that the EC footprint consistently captures a greater impervious surface than the SC footprint. Furthermore, building characteristics in the EC footprint are

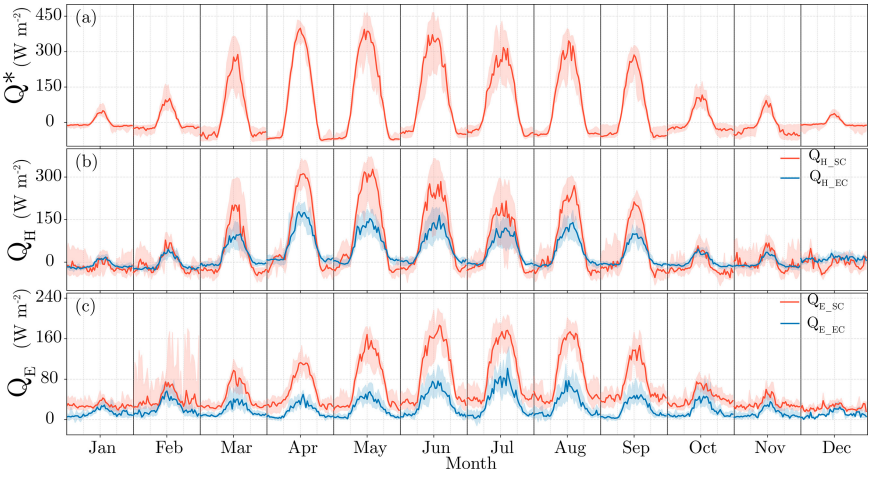


FIG. 7. Monthly median diurnal cycle of net radiation (W m^{-2}) and turbulent fluxes (W m^{-2}): (a) Q^*, (b) Q_{H_SC} and Q_{H_EC}, and (c) Q_{E_SC} and Q_{E_EC}. The median is shown in red; the interquartile range is shown in shading.

Brought to you by provisional account | Unauthenticated | Downloaded 11/17/26 02:09 PM UTC

TABLE 4. (a) Footprint-weighted land-cover fractions and (b) building morphology characteristics within the SC and EC footprints for different WDs.

(a) Land-cover fractions (%)

	EC				SC			
WD	Building	Road	Industrial	Urban green	Building	Road	Industrial	Urban green
NE	36.33	14.47	48.74	0.44	62.41	15.36	11.62	4.01
N	30.65	18.64	49.84	0.92	58.80	14.57	12.38	3.78
E	34.16	14.15	51.23	0.43	63.43	15.45	11.15	4.55
S-SW	33.56	12.76	53.29	0.38	54.16	14.12	17.86	9.66

(b) Building morphology characteristics (m)

	EC			SC		
WD	$\overline{H}$	σ_H	H_{Max}	$\overline{H}$	σ_H	H_{Max}
NE	8.53	6.05	90.83	5.98	3.85	39.57
N	10.31	6.54	50.17	6.12	3.86	39.57
E	9.11	7.16	90.83	6.01	3.72	42.85
S-SW	8.19	6.84	90.83	7.02	4.46	53.86

higher with $\overline{H}$, σ_H, and H_{Max} all substantially larger, than those in the SC footprint. For the majority of dominant WDs, the EC and SC footprints sample largely distinct regions, with only occasional slight overlap. Apart from the flow distortion, differences in the EC and SC footprints are likely a contributor to the observed flux differences between the two systems.

4) SYSTEMATIC DIFFERENCES BETWEEN EC AND SC FLUXES

Turbulent fluxes from EC and SC exhibit similar seasonal patterns; however, systematic differences are present. SC fluxes show higher average values than EC, with the maximum difference at peak solar heating (Fig. 7). From a statistical perspective, during daytime Q_{H_SC} versus Q_{H_EC} and Q_{E_SC} versus Q_{E_EC} (Fig. 9) show R^2 values of 0.68 and 0.28, respectively, and during nighttime $R^2 = 0.09$ and 0.11, respectively (figure not shown). The Q_{H_SC} shows a bias of 36.64 W m^{-2} relative to EC, an RMSE of 82.97 W m^{-2}, and an index of agreement (IoA) of 0.58. For Q_E, the bias is 49.99 W m^{-2}, RMSE is 69.13 W m^{-2}, and IoA is 0.32. Here, IoA is a dimensionless metric (0–1) quantifying the degree to which observations match the temporal pattern and variability of reference observations, with 1 indicating perfect agreement and 0 indicating complete disagreement.

The R^2 values obtained in this study are comparable to those reported in previous urban and suburban SC–EC intercomparison studies. In London, measurements using three scintillometers [one boundary layer scintillometer (BLS) and two LASs] showed moderate agreement between scintillometer-derived and EC-derived sensible heat fluxes, with a mean daytime R^2 of approximately 0.5. This relatively lower agreement was attributed to differences in the EC and scintillometer source areas, as the respective footprints sampled different regions of the heterogeneous urban landscape (Crawford et al. 2017). A long-term urban scintillometer study conducted in Łódź, Poland, reported stronger agreement, with R^2 values of 0.84 and 0.88 between SC and EC for Q_H measurements from two EC stations located within different parts of the scintillometer footprint (Zieliński et al. 2013). Similarly, an intercomparison study over a suburban area of Swindon, United Kingdom, found high correlations between EC and scintillometer Q_H estimates, with R^2 values of 0.86 and 0.87 for BLS and

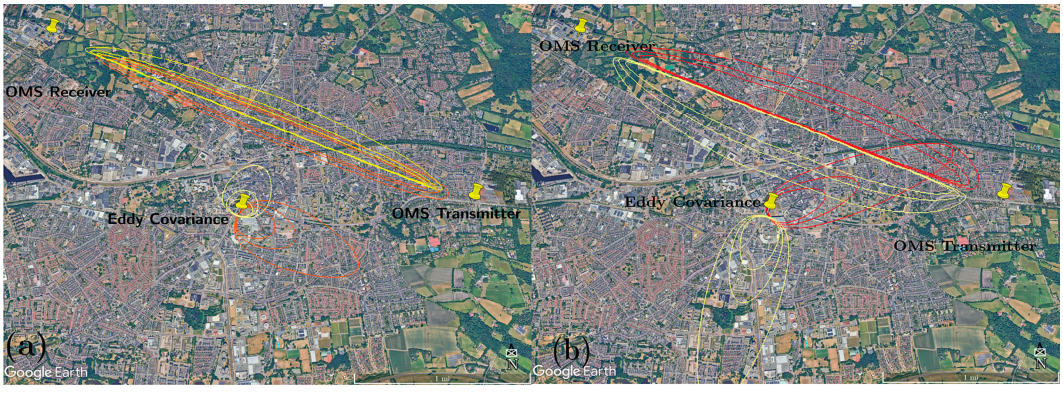


FIG. 8. Example footprints at 1200 local time for different WDs. (a) Yellow: N, red dash: E; (b) red: NE, yellow dash: SW. Contours show 70%–90%.

Brought to you by provisional account | Unauthenticated | Downloaded 11/17/26 02:09 PM UTC

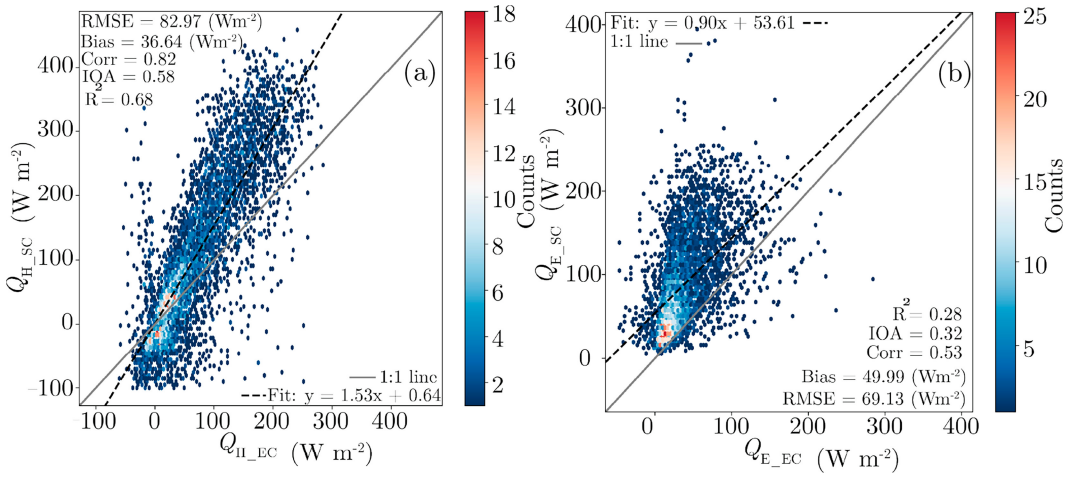


FIG. 9. Hex bin plots for EC and SC observed fluxes during daytime: (a) Q_H and (b) Q_E.

LAS measurements, respectively. For a relatively homogeneous site, Lagouarde et al. (2006) reported that LAS measurements underestimated fluxes by about 4% under daytime conditions compared to EC observations over Marseille. Compared to these findings, our results indicate a substantially larger bias in SC relative to EC.

While footprint characteristics can partially explain these differences, attributing them solely to footprint differences would be an oversimplification process. The presented footprints represent only dominant wind conditions and may vary considerably at shorter temporal scales. Additional sources of uncertainty including limitations in footprint modeling, potential inaccuracies in land-use/land-cover (LULC) classification, and the inherent heterogeneity of urban environments further complicate the interpretation. Methodological differences also play a role: Mauder et al. (2008) and Engelmann and Bernhofer (2016) show that temporal averaging approaches such as eddy covariance may not fully capture the complete spectrum of turbulence, potentially leading to underestimation of turbulent fluxes compared to spatially integrating techniques such as scintillometry. Taken together, these factors highlight that caution is required when drawing definitive conclusions and that the observed discrepancies likely arise from a combination of measurement, methodological, and representativeness uncertainties. And most importantly, in rooftop EC observations carried out over a tall building, the EC measurements could be subjected to flow distortion and the influence of this cannot be ruled out.

4. Vertical flux divergence and flow distortion effects on EC flux measurements

a. *Evidence of vertical flux divergence*

The EC technique is widely recognized as the most reliable method for estimating turbulent fluxes (Foken et al. 2004; Aubinet et al. 2012) and is commonly used as a reference to evaluate scintillometer measurements (e.g., Grimmond et al. 2004; Ward et al. 2014, 2015b). However, in urban areas, the site of flux towers must be carefully chosen (Feigenwinter et al. 2012). It is generally advised to position flux measurements above the roughness sublayer (RSL), often at a height of 2–5 times the $\overline{H}$ (Raupach et al. 1991). Above this height, measurements are typically expected to be in the inertial sublayer (ISL) where vertical flux divergence is negligible (Stull 2012). Below this level, however, roughness-induced flow distortion, shear layer, wakes, organized motions, and heterogeneity substantially influence the observations, resulting in enhanced spatial and temporal variability (Feigenwinter et al. 2012; Rotach 1999). Consequently, the observations become increasingly controlled by local roughness elements close to the rooftop and upwind source-area characteristics, reducing their representativeness of the spatially averaged surface–atmosphere exchange. As we measure turbulent fluxes at two heights, our dataset provides us the unique opportunity to quantify the annual variation of vertical flux divergence.

The $\overline{H}$ in the vicinity of the ITC hotel building is 14 m, with EC instruments installed at approximately $4\overline{H}$ (51 and 56 m AGL). According to boundary layer theory, fluxes in the ISL do not vary appreciably with height (Stull 2012). However, our measurements show systematic flux divergence, with fluxes at 10-m height generally larger in magnitude than the fluxes at 5-m height (Fig. 10).

To investigate this further and to assess whether this is associated with any prevailing WD, we constructed a polar scatterplot of u and WD, with colors indicating difference in the fluxes at the two heights [i.e., Q_H (10 m)–Q_H (5 m); Fig. 11]. The analysis was carried out separately for each season and for stable and unstable atmospheric conditions. For each plot, we also report the percentage of positive and negative flux divergence. The results show that, under unstable conditions, positive flux divergence dominates, indicating that Q_H at 10 m is generally larger than at 5 m. Under stable conditions, when both levels have negative flux values, the upper-level measurements are consistently more negative than the lower-level measurements, resulting in negative flux divergence. These findings align with Grimmond et al. (2004), who demonstrated

Brought to you by provisional account | Unauthenticated | Downloaded 11/17/26 02:09 PM UTC

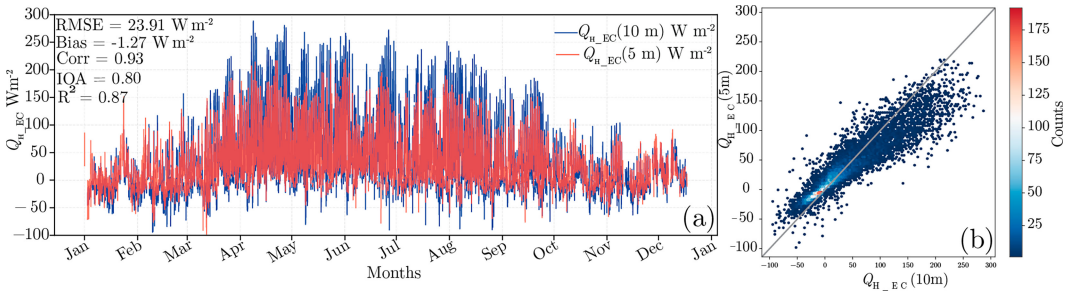


FIG. 10. The Q_H from a two-level EC system at 5 and 10 m above the building roof.

that when both sensors were above the RSL, the ratio of upper to lower Q_H was close to unity. However, when the lower sensor was within the RSL, the ratio exceeded unity. In our case, particularly during the summer months and under both stability regimes, the ratio frequently exceeds one. This shows that the RSL likely influences the EC measurements at the lower measurement height. The systematic flux divergence observed in our measurements is indicative of flow distortion at the lower EC level, which we explore further in the following section.

b. *Flow distortion diagnostics*

Although RSL influence at the lower EC level is evident from the flux divergence analysis, similar conclusions cannot

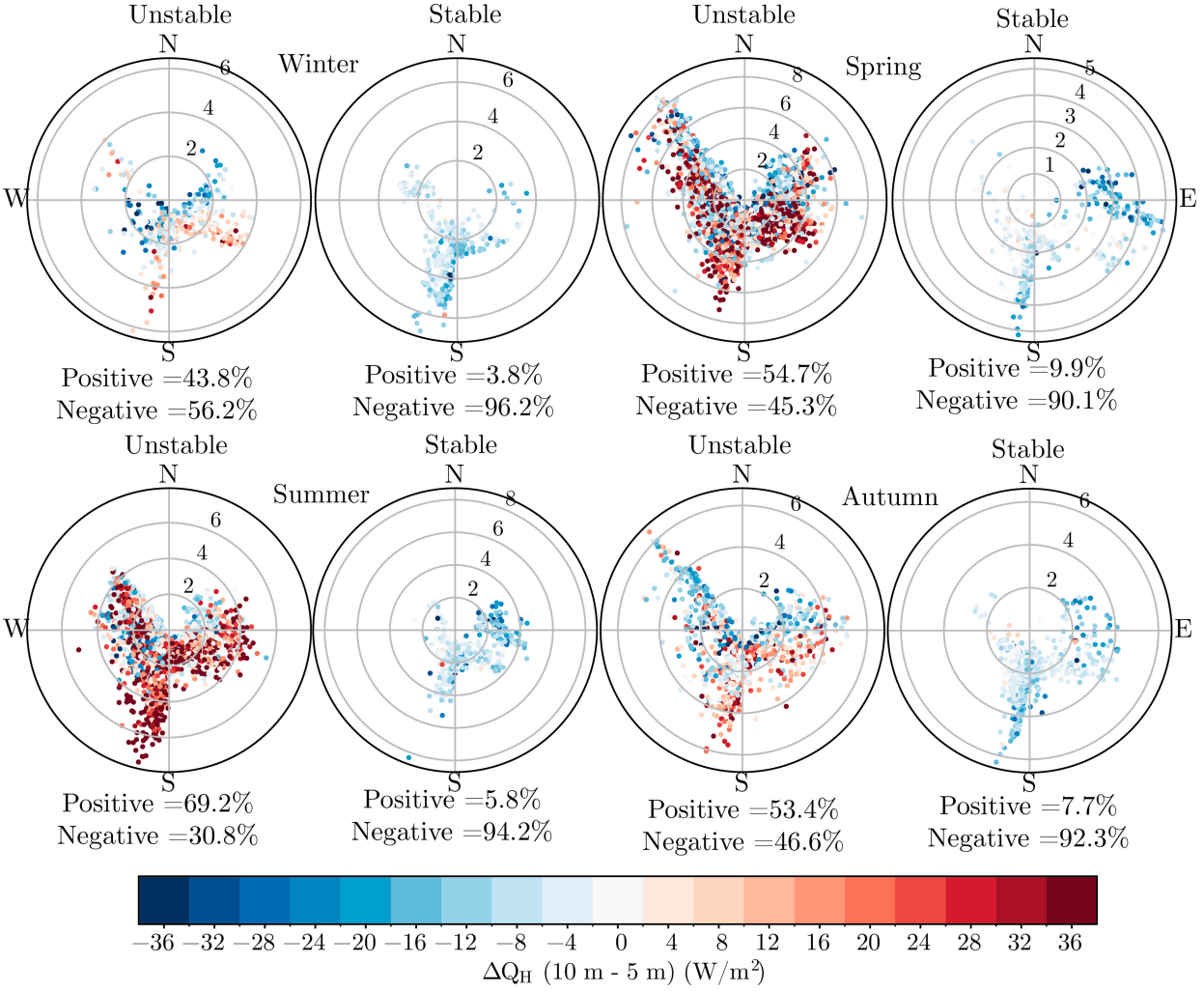


FIG. 11. Polar scatterplot of u and WD, with point color indicating the difference between 10- and 5-m EC observation of Q_H.

Brought to you by provisional account | Unauthenticated | Downloaded 11/17/26 02:09 PM UTC

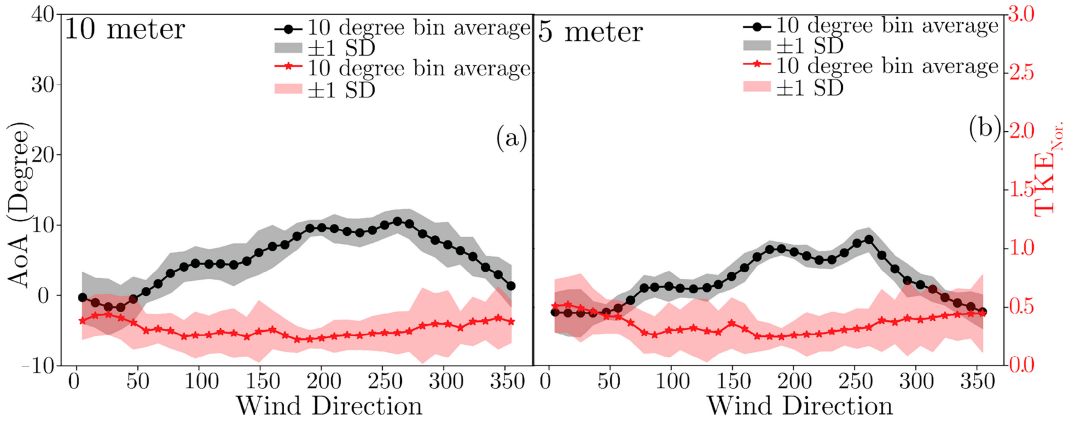


FIG. 12. Flow distortion at both EC levels expressed as (a) AoA and (b) $TKE_{Nor.}$ as a function of WD (0°–360°, where 0° corresponds to N). Lines and symbols represent 15° bin averages; shaded areas indicate ±1 standard deviation.

be drawn directly about the 10-m level, as no additional flux measurement above it is available. To attribute the physical cause of the observed flux divergence, we examine the AoA of the mean streamlines and $TKE_{Nor.}$, following the approaches of Feigenwinter et al. (2012) and Järvi et al. (2018). The AoA, defined as $\text{AoA} = \tan^{-1}(w/\sqrt{u^2 + v^2})$, quantifies the deviation of the mean flow from horizontal. In the ISL, mean streamlines are approximately parallel to the surface and AoA is near zero, whereas nonzero AoA indicates flow distortion consistent with RSL influence. The normalized TKE, $TKE_{Nor.} = 0.5(u'^2 + v'^2 + w'^2)^{1/2}/\overline{u}$, provides a complementary measure of turbulence intensity relative to the mean flow, with strong WD-dependent spikes indicating preferential flow distortion (Järvi et al. 2018). Together, these two diagnostics allow us to assess the degree and directional dependence of flow distortion at each level and thereby attribute the origin of the observed flux divergence.

Figure 12 shows AoA and $TKE_{Nor.}$ at both levels, with 10° bin averages and ±1 standard deviation. Both levels exhibit nonzero AoA across most WDs, with values predominantly between −5° and 15°. This range is generally considered to be representative of the lower flow distortion in typical urban environments (Feigenwinter et al. 2012). The 5-m level exhibits markedly sharper WD-dependent variability in both AoA and $TKE_{Nor.}$ compared to the 10-m level, reflecting stronger sensitivity to nearby roughness elements, wakes, and recirculation zones. This directional sensitivity is physically consistent with a measurement height that is periodically within or near the RSL, where individual roughness elements exert a direct influence on the local flow structure. The 10-m level, by contrast, shows smoother directional behavior and slightly higher AoA, consistent with its proximity to the canopy-top shear layer where turbulence production and vertical velocity fluctuations peak near or slightly above the canopy height (Finnigan et al. 2003; Raupach et al. 1996; Roth 2000).

EC observations at the Enschede site clearly indicate the presence of flow distortion. However, the observed AoA values, along with $TKE_{Nor.}$, predominantly fall within the reported range for urban area, e.g., Järvi et al. (2018) reported AoA values between 5°–18° and 5°–15° outside strongly distorted flow sectors, while $TKE_{Nor.}$ reached up to 2.5 and 1.7 for distorted flow sectors of two EC systems mounted on opposite sides of a tower in Helsinki. Despite these references, there is no widely accepted threshold for AoA in urban environments, and quality-control criteria vary across studies (e.g., Järvi et al. 2018; Horne et al. 2026). Nevertheless, the AoA range observed in this study from −5° to 15° lies well within values commonly reported in the literature and can be considered typical for urban conditions. To limit the influence of extreme flow distortion, additional filtering was applied by excluding averaging periods in which more than 10% of wind vectors exceeded |AoA| of 15°. It should also be noted that, for the CSAT3 sonic anemometer, measurements at $|\text{AoA}| < 15°$ may still underestimate w' by approximately 6%–10% (Frank et al. 2013). This potential bias should be considered when interpreting flux magnitudes.

5. Sensitivity of scintillometer fluxes to input parameters

The SC provides spatially integrated estimates of turbulent fluxes over relatively large areas. City-scale spatially averaged fluxes makes SC particularly well suited for the validation of NWP models, as well as satellite-derived products. However, the derivation of fluxes from SC requires several input parameters, including z_{eff}, aerodynamic roughness parameters (z_0 and z_d), and meteorological variables. Over heterogeneous urban areas, obtaining a single representative values for these parameters is difficult due to the complexity and variability of the surface. This can introduce substantial uncertainty in the estimated fluxes. Therefore, when using SC observations, it is essential to quantify and account for the sensitivity of the flux estimates to these input parameters. This discussion presents an analysis aimed at assessing the magnitude of such uncertainties specifically in heterogeneous urban settings.

a. *Effect of roughness parameters (z_0 and z_d) on SC fluxes*

Turbulent fluxes from SC are estimated using MOST (Monin and Obukhov 1954), which requires aerodynamic roughness

Brought to you by provisional account | Unauthenticated | Downloaded 11/17/26 02:09 PM UTC

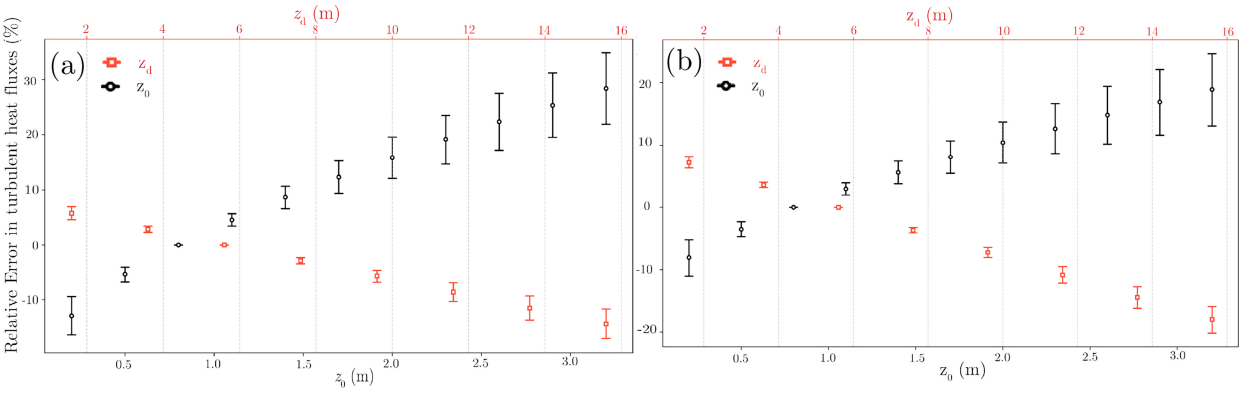


FIG. 13. Sensitivity of SC-derived turbulent fluxes with respect to z_0 and z_d. Black circles (primary x axis) represent sensitivity to z_0, while red squares (secondary x axis) represent sensitivity to z_d. Error bars indicate standard deviation. (a) Sensitivity for 19 Apr. (b) Sensitivity for 5 Aug.

parameters as key inputs. As explained in section 2e, for deriving Q_H and Q_E, an estimate of u_* needs to be provided as an input. The value of u_* [Eq. (8)] depends on both z_0 and z_d. The displacement height z_d further influences the flux estimates as it appears also as an input for calculating z_{eff}. Determining exact roughness parameters for an entire city through experimentation is practically impossible. To address this, various empirical and parameterization schemes (Raupach 1994; Macdonald et al. 1998; Kanda et al. 2013) have been developed. However, obtaining appropriate values for an urban area remains a challenge, as different methods often yield a wide range of values (Kent et al. 2017). To understand the sensitivity of the flux estimates to the choice of parameterizations, we used two parameterizations: (i) a widely used simple "rule of thumb" (Raupach 1994) method and (ii) an aerodynamic parameterization derived using large-eddy simulation (LES; Kanda et al. 2013). For the most frequent southwest winds (~220°), the estimated z_0 values were 0.79 and 1.6 m, and z_d values were 5.5 and 12.87 m, respectively. This simple comparison highlights that parameter estimates from different parameterizations may differ significantly.

Such uncertainties in roughness parameters can lead to significant differences in flux estimates. For example, in Marseille (Lagouarde et al. 2006), with wind measurement heights z_u of 37.9 and 43.9 m, varying z_0 from 0.5 to 2.0 m, using 1.0 m as the reference value, resulted in relative flux differences of 24% (ranging from −8.6% for 0.5 m to 15.4% for 2.0 m) and 10.8% (from −3.8% to 7.0%), respectively. Similarly, varying z_d from 11 to 26 m, with the reference value fixed, produced relative errors of 12.6% (from −2.8% to 9.8%) and 3.2% (from −0.9% to 2.3%). In contrast, Crawford et al. (2017) reported smaller sensitivity for London city, where the measurements at an effective height of 87.76 m and perturbations of z_0 by ±0.25 m (around a reference value of 1.47 m) resulted in approximately ±1% variation in Q_H, while perturbations of z_d by ±0.5 m (around 10.29 m) led to ±0.75% variation. These differences highlight that the sensitivity of flux estimates to roughness parameter uncertainty is strongly site dependent and varies with the beam height and wind measurement height.

To quantify the sensitivity of turbulent fluxes estimates arising from differences in roughness parameters, a sensitivity analysis was conducted. Two contrasting days were selected following Gadde et al. (2026) with different turbulence characteristics: (i) a windy spring day with high wind speed on 19 April 2020 and (ii) a calm, hot, low wind speed day on 5 August 2020. SC flux processing was repeated for a range of z_0 and z_d values. Specifically, z_0 was varied from 0.2 to 3.2 m while keeping z_d fixed at 5.6 m, and subsequently, z_d was varied from 1.6 to 15.6 m, while keeping z_0 fixed at 0.8 m. For each 30-min interval of the day, the relative error in Q_H and Q_E was computed with respect to reference conditions (z_0 = 0.8 m and z_d = 5.6 m). The relative error is defined as follows:

$$\text{relative error } Q_H(\%) = \frac{Q_H(z_0) - Q_H(z_{0,\text{ref}})}{Q_H(z_{0,\text{ref}})}. \tag{13}$$

Although Eq. (13) is defined for Q_H and z_0, it was applied analogously to the combinations (Q_H, z_d), (Q_E, z_0), and (Q_E, z_d).

Figures 13a and 13b present the relative error in turbulent fluxes for different values of z_0 and z_d for the 19 April and 5 August cases, respectively. Since both cases show similar results, we only discuss the 19 April case here. The primary x axis shows changes in z_0, while the secondary x axis represents variations in z_d. The y axis indicates the mean of relative error in turbulent fluxes for the entire day, with error bars denoting the standard deviation and thus reflecting variability in relative error over the course of the day. The results show that, within the typical urban range of z_0, the relative error in Q_H increases with increasing z_0, reaching approximately 25% at maximum roughness length. In contrast, the relative error decreases with increasing z_d, reaching values around −15%.

Since z_0 influences u_*, which in turn affects L_o, it indirectly impacts z_{eff}, which varies with atmospheric stability [Eq. (4)]. As a result, the influence of z_0 is not constant throughout the day but varies slightly with stability conditions. However, the magnitude of this variation is small, as indicated by the standard deviation of the relative error. A similar argument applies to z_d, which is incorporated together with z_{eff}. As shown by Hartogensis et al. (2003), under free convection, a relative error in z_{eff} leads to an equal relative error in Q_H, whereas under neutral conditions, the relative error in Q_H is half that

Brought to you by provisional account | Unauthenticated | Downloaded 11/17/26 02:09 PM UTC

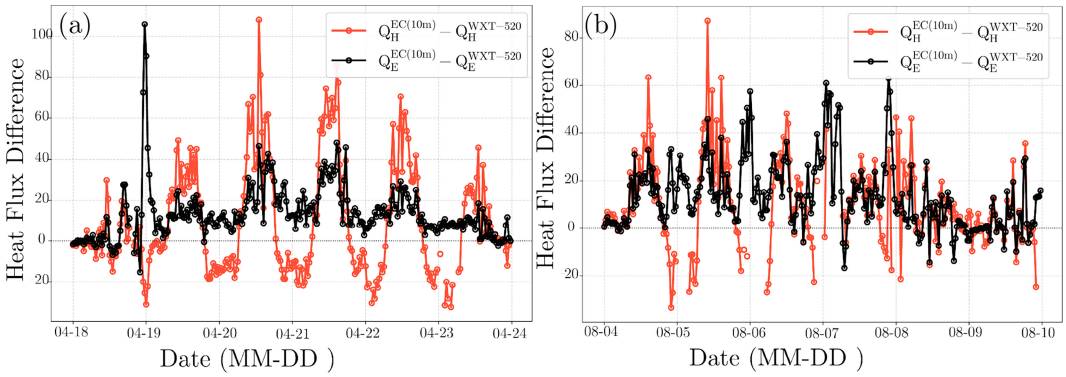


FIG. 14. Difference in SC-derived turbulent fluxes using meteorological observations from the 10-m EC and 2-m WXT520 under two contrasting periods: (a) 18–23 Apr and (b) 4–9 Aug.

of z_{eff}. Therefore, although z_d itself is constant, the resulting effect on Q_H varies slightly over the day due to changes in atmospheric stability. However, its variability is very small. It is also worth noting that z_0 and z_d may vary slightly over the course of the day due to changes in the measurement footprint associated with variations in atmospheric stability, wind speed, and wind direction.

It is important to note that many commonly used parameterization schemes tend to either systematically overestimate or systematically underestimate both z_0 and z_d simultaneously for the Enschede site (see Tables S1 and S2 in the online supplemental material). As a result, an overestimation of z_0, which would independently increase flux estimates, is often partially offset by a concurrent overestimation of z_d, thus moderating the net effect on fluxes. However, this compensation is site specific and depends on the local urban morphology.

b. *Effect of friction velocity input on SC fluxes*

As explained in section 2e, u_* is provided as an input to derive the turbulent fluxes [see Eq. (7)], where u_* is typically derived from Eq. (8) with wind speed as input from meteorological observations. Wind speed for estimating u_* for SC fluxes is typically recorded at either the transmitter or receiver location. However, scintillometers in urban areas are typically installed over building rooftops, and the influence of the building itself on the measured wind speed and thereby on flux estimates cannot be ruled out.

At the Enschede site, both the transmitter and receiver were positioned at the urban periphery to span the entire city; however, this semiurban setting is not fully representative of meteorological conditions in the urban core. Hence, to better capture meteorological conditions over the city, wind speed inputs from the WXT520 sensor from top of the ITC building were used for SC flux calculation. However, as these measurements are carried out at 2 m above the rooftop, they may be influenced by the building itself and can introduce additional uncertainty in the estimation of SC fluxes. In other words, the height at which meteorological measurements are made can influence the SC flux estimates, since wind speed from these measurements is used as an input to calculate u_*.

To demonstrate this height dependence, SC fluxes were estimated using two different wind speed measurements: 1) wind speed from the WXT520 sensor at 2 m above the rooftop and 2) EC measurements at 10 m above the rooftop. This analysis was performed for two contrasting turbulence conditions identified by Gadde et al. (2026): (i) a high wind speed event (18–23 April 2020) and (ii) a calm, low wind speed event (4–9 August 2020). For the EC measurements, high-frequency data were averaged to 1-min intervals for the SC flux analysis.

Figure 14 presents turbulent fluxes from SC, estimated using MOST with wind speed from two different observations. SC fluxes estimated with u_* derived from 10-m EC wind speeds are consistently higher in magnitude than those estimated using wind speeds from the 2-m WXT520 sensor. This difference arises primarily because at 2 m, the wind data are influenced by building-induced shear, leading to lower u_* values and consequently lower flux estimates.

Obviously, flux estimates during the windy spring period (Fig. 14a) show higher sensitivity to the choice of wind speed input than those during the calm, hot summer event (Fig. 14b). This contrast can be understood through the dominant turbulence regime governing each period. During the windy spring event, mechanically driven turbulence dominates, with convective rolls (Gadde et al. 2026) and strong inertial forcing, making u_* the primary scaling variable for turbulent transport. In this regime, any uncertainty in the wind speed input propagates directly and strongly into the u_* estimate and consequently into the derived SC fluxes. In contrast, during the calm summer event, buoyancy-driven convection dominates, with convective cells (Gadde et al. 2026) reducing the relative importance of u_* as a flux-driving variable. Turbulent transport is increasingly governed by the convective velocity scale w_*, which is less sensitive to the horizontal wind speed input. Consequently, the choice of wind speed measurement height has a reduced influence on SC flux estimates under low-wind, convectively driven conditions. This demonstrates that the sensitivity of SC flux estimates to wind speed input uncertainty is regime dependent, being largest when mechanical forcing matters most. Overall, this analysis quantifies potential sources of uncertainty in the scintillometer observations over the Enschede site and explains the reason for using wind data from 10-m EC system to derive the turbulent fluxes for this dataset.

Brought to you by provisional account | Unauthenticated | Downloaded 11/17/26 02:09 PM UTC

6. Conclusions

This study presents a year-long dataset of urban surface–atmosphere energy exchange over Enschede, the Netherlands, obtained using a four-component radiometer in combination with eddy covariance (EC; neighborhood scale) and optical microwave scintillometer (SC; city scale) measurements. The dataset captures the full seasonal cycle of radiative and turbulent fluxes and can support the development, improvement, and validation of parameterizations used in numerical weather prediction (NWP) and climate models and serve as ground truth for satellite observations. Due to its large spatial footprint, the scintillometer is particularly suited for evaluating city-scale simulations such as WRF, providing path-averaged fluxes representative of model grid cells. In contrast, EC measurements, with their smaller and more localized footprint, are better suited for evaluating high-resolution, building-resolving LES.

Overall, radiative fluxes exhibit a clear seasonal cycle, with seasonal Q^* average ranging from -4 W m^{-2} in winter to 90 W m^{-2} in summer, working as a primary source for turbulent fluxes. Although the microscale footprint of the rooftop four-component radiometer limits the spatial representativeness of absolute flux magnitudes, it captures the first-order temporal variability of Q^*. Turbulent fluxes from both EC and SC broadly follow the seasonal and diurnal evolutions of Q^*, with Q_H dominating in spring under dry conditions and a more balanced partitioning between Q_H and Q_E in summer due to increased precipitation and vegetation activity. A notable contrast also emerges in the diurnal patterns: The Q_{H_SC} shows more negative flux values than Q_{H_EC} from late evening to midnight. This likely reflects the rapid radiative cooling of the more vegetated SC footprint, whereas Q_{H_EC} remains positive or near zero due to the higher thermal inertia of the built-up EC footprint, which sustains heat storage release. This contrast highlights the role of measurement footprint in controlling energy partitioning. Results also shows that Q_{H_SC} after midnight tends to remain nearly constant or exhibit a slight continuous increase. This apparent nighttime increase in Q_{H_SC} results from ambiguity in determining the sign of Q_H from r_{Tq}. A positive r_{Tq} does not uniquely indicate positive sensible heat flux, as it can also occur under stable conditions with $Q_H < 0$ and $Q_E < 0$, such as during dew fall (Ward et al. 2015b). Under weak nocturnal turbulence, the small values of C_{Tq} and C_q^2 further increase the uncertainty in the inferred sign (Beyrich et al. 2005). The nighttime sign reversal observed in April and May, without a comparable change in magnitude, therefore reflects uncertainty in the retrieved flux sign rather than a physical change in Q_H. While EC and SC fluxes show good temporal agreement at seasonal scales, SC fluxes are systematically higher in magnitude, with daytime R^2 values of 0.68 for Q_H and 0.28 for Q_E and biases of 36.64 and 49.99 W m^{-2}, respectively. These discrepancies may arise from a combination of factors, including the choice of roughness parameterization schemes used to derive the roughness parameter for the scintillometer, the choice of similarity functions used for scintillometer data derivation, footprint mismatches between the two instruments, and residual flow distortion effects affecting the EC measurements.

The two-level EC setup revealed systematic flux divergence, with fluxes at 10 m consistently larger in magnitude than at 5 m. Flow distortion diagnostics based on angle of attack (AoA) and normalized turbulent kinetic energy ($TKE_{Nor.}$) confirm that both levels are subject to influence from the roughness sublayer (RSL), where proximity roughness elements of rooftop suppress vertical turbulent exchange. Nevertheless, AoA values at both levels fall within $-5°$ and 15°, consistent with values reported in the literature for urban EC measurements, and neither level exhibits the strong $TKE_{Nor.}$ spikes associated with severe flow distortion. The 10-m level, while not entirely free of RSL effects, provides a more spatially integrated and physically consistent estimate of surface–atmosphere exchange and is used exclusively for all EC flux results in this study. There is currently no widely accepted threshold for acceptable AoA in urban environments, and the resulting quantitative impact on flux magnitudes remains poorly quantified, highlighting the need for further research in this area.

Sensitivity analyses show that SC flux estimates are influenced by the aerodynamic roughness parameters z_0 and z_d, which exert opposing effects: Increasing z_0 raises flux estimates by up to 25%, while increasing z_d reduces them by up to 15% across the tested parameter range. Different parameterization schemes often simultaneously overestimate or underestimate both parameters, which can lead to partial error compensation. However, this compensation is site specific and dependent on local urban morphology, limiting its general applicability.

The sensitivity of SC fluxes to the wind speed measurement height is shown to be regime dependent. Under mechanically driven turbulence, where u_* is the primary scaling variable, flux differences of up to 80 W m^{-2} were observed between estimates using wind speed at 2 m versus 10 m. Under buoyancy-dominated convection, where turbulent transport is increasingly governed by the convective velocity scale w_*, this sensitivity is reduced, with differences of around 60 W m^{-2}. This finding underscores the importance of careful site selection for meteorological inputs in scintillometer processing, particularly under windy conditions when the accuracy of u_* matters most.

In conclusion, this study provides a novel multiscale urban flux observation dataset, evaluates the representativeness of multiscale observations, assesses the potential influence of flow distortion, and quantifies the uncertainties associated with input-parameter uncertainties. These uncertainties must be explicitly taken into account when using such measurements to evaluate NWP models or satellite products. Future work should focus on the development of urban-specific AoA quality-control thresholds, improved methods for estimating spatially representative roughness parameters, and coordinated multisite campaigns across contrasting urban morphologies to improve the generalizability of the sensitivity findings reported here.

Acknowledgments. This work was supported by the 4TU Heat Robustness in Relation to Ageing Cities (HERITAGE)

Brought to you by provisional account | Unauthenticated | Downloaded 11/17/26 02:09 PM UTC

program under Grant 4TU-UIT-469, funded by the High Tech for a Sustainable Future (HTSF) initiative of 4TU, the federation of the four technical universities in the Netherlands. We thank the three anonymous reviewers for their valuable comments, which significantly improved this article. We are grateful to Mehmet Büyükdemircioğlu for providing the GIS workflow for determining albedo. We also thank Oscar Hartogensis (MAQ, Wageningen University and Research, the Netherlands) for his insightful suggestions during this work. The authors declare no conflicts of interest.

Data availability statement. The datasets and code used in this study are openly accessible on Zenodo. The data can be found at https://doi.org/10.5281/zenodo.19631675, and the corresponding code is available at https://doi.org/10.5281/zenodo.19632632.

REFERENCES

Andreas, E. L, 1988: Estimating Cn2 over snow and sea ice from meteorological data. *J. Opt. Soc. Amer.*, **5A**, 481–495, https://doi.org/10.1364/JOSAA.5.000481.

Arnfield, A. J., 2003: Two decades of urban climate research: A review of turbulence, exchanges of energy and water, and the urban heat island. *Int. J. Climatol.*, **23** (1), 1–26, https://doi.org/10.1002/joc.859.

Aubinet, M., T. Vesala, and D. Papale, 2012: *Eddy Covariance: A Practical Guide to Measurement and Data Analysis.* Springer, 438 pp., https://doi.org/10.1007/978-94-007-2351-1.

Barlow, J. F., J. Harrison, A. G. Robins, and C. R. Wood, 2011: A wind-tunnel study of flow distortion at a meteorological sensor on top of the BT Tower, London, UK. *J. Wind Eng. Ind. Aerodyn.*, **99**, 899–907, https://doi.org/10.1016/j.jweia.2011.05.001.

Beyrich, F., R. D. Kouznetsov, J. P. Leps, A. Lüdi, W. M. Meijninger, and U. Weisensee, 2005: Structure parameters for temperature and humidity from simultaneous eddy-covariance and scintillometer measurements. *Meteor. Z.*, **14**, 641–649, https://doi.org/10.1127/0941-2948/2005/0064.

Campbell Scientific, 2025a: CNR1: Kipp & Zonen, net radiometer. 40 pp., https://s.campbellsci.com/documents/us/manuals/cnr1.pdf.

——, 2025b: CR1000: Measurement and control datalogger. 588 pp., https://s.campbellsci.com/documents/br/manuals/cr1000.pdf.

Christen, A., and R. Vogt, 2004: Energy and radiation balance of a central European city. *Int. J. Climatol.*, **24**, 1395–1421, https://doi.org/10.1002/joc.1074.

Copernicus Programme, 2018: Urban atlas land cover/land use 2018 (vector), Europe, 6-yearly, Jul. 2021. Copernicus Programme, accessed 2 October 2025, https://doi.org/10.2909/fb4dffa1-6ceb-4cc0-8372-1ed354c285e6.

Crawford, B., C. S. B. Grimmond, H. C. Ward, W. Morrison, and S. Kotthaus, 2017: Spatial and temporal patterns of surface–atmosphere energy exchange in a dense urban environment using scintillometry. *Quart. J. Roy. Meteor. Soc.*, **143**, 817–833, https://doi.org/10.1002/qj.2967.

De Bruin, H., W. Kohsiek, and B. Van Den Hurk, 1993: A verification of some methods to determine the fluxes of momentum, sensible heat, and water vapour using standard deviation and structure parameter of scalar meteorological quantities. *Bound.-Layer Meteor.*, **63**, 231–257, https://doi.org/10.1007/BF00710461.

Engelmann, C., and C. Bernhofer, 2016: Exploring eddy-covariance measurements using a spatial approach: The eddy matrix. *Bound.-Layer Meteor.*, **161**, 1–17, https://doi.org/10.1007/s10546-016-0161-x.

Feigenwinter, C., R. Vogt, and A. Christen, 2012: Eddy covariance measurements over urban areas. *Eddy Covariance: A Practical Guide to Measurement and Data Analysis*, M. Aubinet, T. Vesala, and D. Papale, Eds., Springer, 377–397, https://doi.org/10.1007/978-94-007-2351-1_16.

Finnigan, J. J., R. Clement, Y. Malhi, R. Leuning, and H. Cleugh, 2003: A re-evaluation of long-term flux measurement techniques Part I: Averaging and coordinate rotation. *Bound.-Layer Meteor.*, **107**, 1–48, https://doi.org/10.1023/A:1021554900225.

Flerchinger, G., W. Xaio, D. Marks, T. Sauer, and Q. Yu, 2009: Comparison of algorithms for incoming atmospheric longwave radiation. *Water Resour. Res.*, **45**, W03423, https://doi.org/10.1029/2008WR007394.

Foken, T., M. Göockede, M. Mauder, L. Mahrt, B. Amiro, and W. Munger, 2004: Post-field data quality control, *Handbook of Micrometeorology: A Guide for Surface Flux Measurement and Analysis*, X. Lee, W. Massman, and B. Law, Eds., Springer, 181–208, https://doi.org/10.1007/1-4020-2265-4_9.

Fortuniak, K., W. Pawlak, and M. Siedlecki, 2013: Integral turbulence statistics over a central European city centre. *Bound.-Layer Meteor.*, **146**, 257–276, https://doi.org/10.1007/s10546-012-9762-1.

Frank, J. M., W. J. Massman, and B. E. Ewers, 2013: Underestimates of sensible heat flux due to vertical velocity measurement errors in non-orthogonal sonic anemometers. *Agric. For. Meteor.*, **171–172**, 72–81, https://doi.org/10.1016/j.agrformet.2012.11.005.

Gadde, S., G. J. Steeneveld, and W. Timmermans, 2026: Understanding urban turbulence at hectometric scale using WRF-LES and eddy covariance observations. *Build. Environ.*, **293**, 114365, https://doi.org/10.1016/j.buildenv.2026.114365.

Goldbach, A., and W. Kuttler, 2013: Quantification of turbulent heat fluxes for adaptation strategies within urban planning. *Int. J. Climatol.*, **33**, 143–159, https://doi.org/10.1002/joc.3437.

Grimmond, C. S. B., 2006: Progress in measuring and observing the urban atmosphere. *Theor. Appl. Climatol.*, **84**, 3–22, https://doi.org/10.1007/s00704-005-0140-5.

——, J. Salmond, T. R. Oke, B. Offerle, and A. Lemonsu, 2004: Flux and turbulence measurements at a densely built-up site in Marseille: Heat, mass (water and carbon dioxide), and momentum. *J. Geophys. Res.*, **109**, D24101, https://doi.org/10.1029/2004JD004936.

——, and Coauthors, 2010: Climate and more sustainable cities: Climate information for improved planning and management of cities (producers/capabilities perspective). *Procedia Environ. Sci.*, **1**, 247–274, https://doi.org/10.1016/j.proenv.2010.09.016.

Hartogensis, O. K., 2006: Exploring scintillometry in the stable atmospheric surface layer. Ph.D. thesis, Wageningen University and Research, 240 pp., https://doi.org/10.18174/121762.

——, 2026: Scintillometer sensible and latent heat fluxes at Amsterdam and Cabauw (NL), 2018–2025. Wageningen University and Research, https://doi.org/10.17887/wur01-rijpwg.

——, C. Watts, J. Rodriguez, and H. De Bruin, 2003: Derivation of an effective height for scintillometers: La Poza experiment in northwest Mexico. *J. Hydrometeor.*, **4**, 915–928, https://doi.org/10.1175/1525-7541(2003)004<0915:DOAEHF>2.0.CO;2.

Brought to you by provisional account | Unauthenticated | Downloaded 11/17/26 02:09 PM UTC

Hill, R. J., 1997: Algorithms for obtaining atmospheric surface-layer fluxes from scintillation measurements. *J. Atmos. Oceanic Technol.*, **14**, 456–467, https://doi.org/10.1175/1520-0426(1997)014<0456:AFOASL>2.0.CO;2.

Horne, J. P., S. J. Richardson, S. L. Murphy, H. C. Kenion, B. J. Haupt, B. J. Ahlswede, N. L. Miles, and K. J. Davis, 2026: The INFLUX network—Eddy covariance in and around an urban environment. *Earth Syst. Sci. Data*, **18**, 823–843, https://doi.org/10.5194/essd-18-823-2026.

Huiskamp, A., 2021: Year 2020. KNMI, accessed 23 July 2025, https://www.knmi.nl/nederland-nu/klimatologie/maand-en-seizoensoverzichten/2020/jaar.

Järvi, L., and Coauthors, 2018: Uncertainty of eddy covariance flux measurements over an urban area based on two towers. *Atmos. Meas. Tech.*, **11**, 5421–5438, https://doi.org/10.5194/amt-11-5421-2018.

Kaimal, J., and J. Finnigan, 1994: *Atmospheric Boundary Layer Flows.* Oxford University Press, 289 pp., https://doi.org/10.1002/qj.49712152512.

Kanda, M., A. Inagaki, T. Miyamoto, M. Gryschka, and S. Raasch, 2013: A new aerodynamic parametrization for real urban surfaces. *Bound.-Layer Meteor.*, **148**, 357–377, https://doi.org/10.1007/s10546-013-9818-x.

Kent, C. W., S. Grimmond, J. Barlow, D. Gatey, S. Kotthaus, F. Lindberg, and C. H. Halios, 2017: Evaluation of urban local-scale aerodynamic parameters: Implications for the vertical profile of wind speed and for source areas. *Bound.-Layer Meteor.*, **164**, 183–213, https://doi.org/10.1007/s10546-017-0248-z.

Khor, N. J. K., and Coauthors, 2022: World cities report 2022: Envisaging the future of cities. United Nations Human Settlements Programme (UN-Habitat) Rep., 422 pp., https://digitallibrary.un.org/record/3984713/files/wcr_2022.pdf?version=1.

Kljun, N., P. Calanca, M. Rotach, and H. P. Schmid, 2015 A simple two-dimensional parameterisation for Flux Footprint Prediction (FFP). *Geosci. Model Dev.*, **8**, 3695–3713, https://doi.org/10.5194/gmd-8-3695-2015.

Klok, L., S. Zwart, H. Verhagen, and E. Mauri, 2012: The surface heat island of Rotterdam and its relationship with urban surface characteristics. *Resour. Conserv. Recycl.*, **64**, 23–29, https://doi.org/10.1016/j.resconrec.2012.01.009.

KNMI, 2020: KNMI weather station data. Koninklijk Nederlands Meteorologisch Instituut, accessed 2 February 2025, https://www.daggegevens.knmi.nl/klimatologie/uurgegevens.

Kottek, M., J. Grieser, C. Beck, B. Rudolf, and F. Rubel, 2006: World map of the Köppen-Geiger climate classification updated. *Meteor. Z.*, **15**, 259–263, https://doi.org/10.1127/0941-2948/2006/0130.

Kotthaus, S., and C. S. B. Grimmond, 2014a: Energy exchange in a dense urban environment—Part I: Temporal variability of long-term observations in central London. *Urban Climate*, **10**, 261–280, https://doi.org/10.1016/j.uclim.2013.10.002.

——, and ——, 2014b: Energy exchange in a dense urban environment—Part II: Impact of spatial heterogeneity of the surface. *Urban Climate*, **10**, 281–307, https://doi.org/10.1016/j.uclim.2013.10.001.

Lagouarde, J. P., M. Irvine, J. M. Bonnefond, C. Grimmond, N. Long, T. Oke, J. Salmond, and B. Offerle, 2006: Monitoring the sensible heat flux over urban areas using large aperture scintillometry: Case study of Marseille city during the Escompte experiment. *Bound.-Layer Meteor.*, **118**, 449–476, https://doi.org/10.1007/s10546-005-9001-0.

Li, D., E. Bou-Zeid, and H. A. De Bruin, 2012: Monin–Obukhov similarity functions for the structure parameters of temperature and humidity. *Bound.-Layer Meteor.*, **145**, 45–67, https://doi.org/10.1007/s10546-011-9660-y.

Li, Z. L., R. Tang, Z. Wan, Y. Bi, C. Zhou, B. Tang, G. Yan, and X. Zhang, 2009: A review of current methodologies for regional evapotranspiration estimation from remotely sensed data. *Sensors*, **9**, 3801–3853, https://doi.org/10.3390/s90503801.

Lindberg, F., and Coauthors, 2018: Urban Multi-scale Environmental Predictor (UMEP): An integrated tool for city-based climate services. *Environ. Modell. Software*, **99**, 70–87, https://doi.org/10.1016/j.envsoft.2017.09.020.

Lowry, W. P., 1977: Empirical estimation of urban effects on climate: A problem analysis. *J. Appl. Meteor.*, **16**, 129–135, https://doi.org/10.1175/1520-0450(1977)016<0129:EEOUEO>2.0.CO;2.

Lüdi, A., F. Beyrich, and C. Mätzler, 2005: Determination of the turbulent temperature–humidity correlation from scintillometric measurements. *Bound.-Layer Meteor.*, **117**, 525–550, https://doi.org/10.1007/s10546-005-1751-1.

Macdonald, R., R. Griffiths, and D. Hall, 1998: An improved method for the estimation of surface roughness of obstacle arrays. *Atmos. Environ.*, **32**, 1857–1864, https://doi.org/10.1016/S1352-2310(97)00403-2.

Mauder, M., R. Desjardins, E. Pattey, Z. Gao, and R. Van Haarlem, 2008: Measurement of the sensible eddy heat flux based on spatial averaging of continuous ground-based observations. *Bound.-Layer Meteor.*, **128**, 151–172, https://doi.org/10.1007/s10546-008-9279-9.

Meijninger, W., O. Hartogensis, W. Kohsiek, J. Hoedjes, R. Zuurbier, and H. De Bruin, 2002: Determination of area-averaged sensible heat fluxes with a large aperture scintillometer over a heterogeneous surface—Flevoland field experiment. *Bound.-Layer Meteor.*, **105**, 37–62, https://doi.org/10.1023/A:1019647732027.

Michel, D., R. Philipona, C. Ruckstuhl, R. Vogt, and L. Vuilleumier, 2008: Performance and uncertainty of CNR1 net radiometers during a one-year field comparison. *J. Atmos. Oceanic Technol.*, **25**, 442–451, https://doi.org/10.1175/2007JTECHA973.1.

Moncrieff, J., R. Clement, J. Finnigan, and T. Meyers, 2004: Averaging, detrending, and filtering of eddy covariance time series. *Handbook of Micrometeorology: A Guide for Surface Flux Measurement and Analysis*, X. Lee, W. Massman, and B. Law, Eds., Springer, 7–31, https://doi.org/10.1007/1-4020-2265-4_2.

Monin, A., and A. Obukhov, 1954: Osnovnye zakonomernosti turbulentnogo peremeshivanija v prizemnom sloe atmosfery (basic laws of turbulent mixing in the atmosphere near the ground). *Tr. Geofiz. Inst. Akad. Nauk SSSR*, **24**, 163–187.

Offerle, B., C. S. B. Grimmond, and K. Fortuniak, 2005: Heat storage and anthropogenic heat flux in relation to the energy balance of a central European city centre. *Int. J. Climatol.*, **25**, 1405–1419, https://doi.org/10.1002/joc.1198.

——, ——, ——, K. Kłysik, and T. R. Oke, 2006a: Temporal variations in heat fluxes over a central European city centre. *Theor. Appl. Climatol.*, **84**, 103–115, https://doi.org/10.1007/s00704-005-0148-x.

——, ——, ——, and W. Pawlak, 2006b: Intraurban differences of surface energy fluxes in a central European city. *J. Appl. Meteor. Climatol.*, **45**, 125–136, https://doi.org/10.1175/JAM2319.1.

Oke, T. R., G. Mills, A. Christen, and J. A. Voogt, 2017: *Urban Climates.* Cambridge University Press, 525 pp., https://doi.org/10.1017/9781139016476.

Overheid, 2020: Current Height File Netherlands (AHN) DSM. Rijkswaterstaat (Netherlands), accessed 31 October 2025,

Brought to you by provisional account | Unauthenticated | Downloaded 11/17/26 02:09 PM UTC

https://data.europa.eu/88u/dataset/36461-actueel-hoogtebestand-nederland-dsm-ahn4-.

——, 2023: Current Height File Netherlands (AHN) DTM. Rijkswaterstaat (Netherlands), accessed 31 October 2025, https://data.europa.eu/88u/dataset/41daef8b-155e-4608-b49c-c87ea45d931c.

Radiometer Physics, 2018: Microwave scintillometer operation & software guide version 2.11. Radiometer Physics, a Rohde & Schwarz Company, Doc. RPG-MWSC-160, 70 pp., https://www.radiometer-physics.de/download/PDF/Scintillometer/RPG-MWSC-160_Instrument_Manual.pdf.

Rahman, M. M., and W. Zhang, 2019: Validation of satellite-derived sensible heat flux for TERRA/MODIS images over three different landscapes using large aperture scintillometer and eddy covariance measurements. *IEEE J. Sel. Top. Appl. Earth Obs. Remote Sens.*, **12**, 3327–3337, https://doi.org/10.1109/JSTARS.2019.2928880.

Raupach, M. R., 1994: Simplified expressions for vegetation roughness length and zero-plane displacement as functions of canopy height and area index. *Bound.-Layer Meteor.*, **71**, 211–216, https://doi.org/10.1007/BF00709229.

——, R. A. Antonia, and S. Rajagopalan, 1991: Rough-wall turbulent boundary layers. *Appl. Mech. Rev.*, **44** (1), 1–25, https://doi.org/10.1115/1.3119492.

——, J. J. Finnigan, and Y. Brunei, 1996: Coherent eddies and turbulence in vegetation canopies: The mixing-layer analogy. *Bound.-Layer Meteor.*, **78**, 351–382, https://doi.org/10.1007/BF00120941.

Rotach, M. W., 1999: On the influence of the urban roughness sublayer on turbulence and dispersion. *Atmos. Environ.*, **33**, 4001–4008, https://doi.org/10.1016/S1352-2310(99)00141-7.

Roth, M., 2000: Review of atmospheric turbulence over cities. *Quart. J. Roy. Meteor. Soc.*, **126**, 941–990, https://doi.org/10.1002/qj.49712656409.

Saunders, B., S. Grimmond, D. Hertwig, S. I. Bohnenstengel, H. W. Lean, and W. Morrison, 2024: Methodology to evaluate numerical weather predictions using large-aperture scintillometry sensible heat fluxes: Demonstration in London. *Quart. J. Roy. Meteor. Soc.*, **150**, 4709–4736, https://doi.org/10.1002/qj.4837.

Stull, R. B., 2012: *An Introduction to Boundary Layer Meteorology*. Atmospheric and Oceanographic Sciences Library, Vol. 13, Springer, 670 pp., https://doi.org/10.1007/978-94-009-3027-8.

Tirel, P. A., A. Perrot, R. Baudet, and D. Rangeard, 2025: Field and laboratory characterization of the albedo of asphalt and horizontal surfaces. *Mater. Struct.*, **58**, 262, https://doi.org/10.1617/s11527-025-02787-7.

Vaisala, 2012: Vaisala weather transmistter WXT520, 171 pp., https://www.vaisala.com/sites/default/files/documents/M210906EN-C.pdf.

Vesala, T., and Coauthors, 2008: Surface–atmosphere interactions over complex urban terrain in Helsinki, Finland. *Tellus*, **60B**, 188–199, https://doi.org/10.1111/j.1600-0889.2007.00312.x.

Ward, H. C., 2017: Scintillometry in urban and complex environments: A review. *Meas. Sci. Technol.*, **28**, 064005, https://doi.org/10.1088/1361-6501/aa5e85.

——, J. G. Evans, and C. S. B. Grimmond, 2014: Multi-scale sensible heat fluxes in the suburban environment from large-aperture scintillometry and eddy covariance. *Bound.-Layer Meteor.*, **152**, 65–89, https://doi.org/10.1007/s10546-014-9916-4.

——, ——, ——, and J. Bradford, 2015a: Infrared and millimetre-wave scintillometry in the suburban environment—Part 1: Structure parameters. *Atmos. Meas. Tech.*, **8**, 1385–1405, https://doi.org/10.5194/amt-8-1385-2015.

——, ——, and ——, 2015b: Infrared and millimetre-wave scintillometry in the suburban environment—Part 2: Large-area sensible and latent heat fluxes. *Atmos. Meas. Tech.*, **8**, 1407–1424, https://doi.org/10.5194/amt-8-1407-2015.

Weber, S., and K. Kordowski, 2010: Comparison of atmospheric turbulence characteristics and turbulent fluxes from two urban sites in Essen, Germany. *Theor. Appl. Climatol.*, **102**, 61–74, https://doi.org/10.1007/s00704-009-0240-8.

Winck, B. R., J. M. Bloor, and K. Klumpp, 2023: Eighteen years of upland grassland carbon flux data: Reference datasets, processing, and gap-filling procedure. *Sci. Data*, **10**, 311, https://doi.org/10.1038/s41597-023-02221-z.

Zhou, Y., S. Marathe, M. Zeman, O. Isabella, and H. Ziar, 2025: Assessing the dual radiative consequences of urban PV integration: Albedo change and radiative forcing dynamics. *Appl. Energy*, **401**, 126544, https://doi.org/10.1016/j.apenergy.2025.126544.

Zieliński, M., K. Fortuniak, W. Pawlak, and M. Siedlecki, 2013: Turbulent sensible heat flux in Łódź, Central Poland, obtained from scintillometer and eddy covariance measurements. *Meteor. Z.*, **22**, 603–613, https://doi.org/10.1127/0941-2948/2013/0448.

Brought to you by provisional account | Unauthenticated | Downloaded 11/17/26 02:09 PM UTC